DOI: https://doi.org/10.2138/am-2023-9296. http://www.minsocam.org/

Revision 1

The transition of the magma plumbing system of Tianchi shield-forming basalts, Changbaishan Volcanic Field, NE China: Constraints from dynamic Fe-Mg diffusion modelling in olivine

Ye Tian[1], Tong Hou[1, 2, 3*], Meng Wang[1], Ronghao Pan[1, 3], Xudong Wang[1], Felix Marxer[3]

1. *Frontiers Science Center for Deep-time Digital Earth, China University of Geosciences (Beijing), Beijing 100083, China*
2. *Key Laboratory of Intraplate Volcanoes and Earthquakes, China University of Geosciences, Beijing, Ministry of Education, Beijing 100083, China*
3. *Institute of Mineralogy, Leibniz Universität Hannover, Callinstr. 3, 30167, Hannover, Germany.*

Correspondence to Dr. Tong Hou (E-mail address: thou@cugb.edu.cn)

DOI: https://doi.org/10.2138/am-2023-9296. http://www.minsocam.org/

ABSTRACT

The depths of crustal reservoirs within volcanic systems may experience transitions over time. Here, we report the crystal and bulk rock compositions of the shield-forming basaltic lavas of the Tianchi composite volcano in the intraplate Changbaishan Volcanic Field, NE China to constrain the crustal magmatic evolution with time. We investigated samples covering the entire basaltic stratigraphic sequence, consisting of the Toudao (TD), Baishan (BS), and Laofangzixiaoshan (LFZ) units from bottom to top, respectively. The core compositions of olivine macrocrysts vary among the three units, i.e., the TD and BS olivine phenocrysts can both be divided into two populations: a high-Fo population (~$Fo_{76\text{-}80}$) and a low-Fo population (~$Fo_{72\text{-}74}$). The LFZ unit only exhibits a high-Fo population (~$Fo_{77\text{-}80}$). Phase equilibria modelling using rhyolite-MELTS suggests that the high-Fo populations were stored at depths of ~20 km for the TD and BS units and ~15 km for the LFZ unit. The low-Fo populations crystallized at shallow depths, i.e., ≤15 km for the TD unit and ≤13 km for the BS unit. We employ a dynamic Fe-Mg interdiffusion modelling with constantly adapting boundary conditions in zoned olivine macrocrysts to constrain the magmatic environments and timescales during the pre-eruption and post-eruption, enabling clarify the magmatic histories recorded by two olivine populations. The dynamic Fe-Mg interdiffusion modelling considers the variable boundary condition caused by crystal growth and composition variation of melts during magma cooling. Calculated results suggest that the high-Fo populations from the TD and BS units recorded prolonged timescales ranging from six months to more than two years with lower cooling rates and slower crystal growth rates. These characteristics reflect a relatively hot and slow-cooling magmatic environment; and the modelled timescales correspond to the sum time including shallow storage, magma ascent, and further cooling within the lava flows. Conversely, the high-Fo population from the LFZ unit and the low-Fo populations from the TD and BS units record shorter timescales (<140 days) with higher cooling rates and faster crystal growth rates. These results indicate relatively cold and highly undercooling magmatic environments; hence the timescales record magma ascent in the conduits and further cooling during lava emplacements. Our study demonstrates that the Tianchi basaltic plumbing system experienced a structural transition over time. In detail, the TD and BS magmas experienced multi-stage stalling and ascent, first accumulating in deep reservoirs and then transferring to shallow reservoirs for storage before the eruption. The LFZ magmas accumulated in a mid-crustal reservoir, followed by a direct ascent to the surface without additional residence.

Key words: Changbaishan; volcano; olivine; diffusion; magma plumbing system

This is the peer-reviewed, final accepted version for American Mineralogist, published by the Mineralogical Society of America.
The published version is subject to change. Cite as Authors (Year) Title. American Mineralogist, in press.
DOI: https://doi.org/10.2138/am-2023-9296. http://www.minsocam.org/

INTRODUCTION

Understanding the timeframes of pre-, syn-, and post-eruptive processes, such as how often the magmatic systems are reactivated or how fast ascending magmas are transported from crustal reservoirs to the surface, is a key subject in modern volcanology. Recent studies on basaltic systems in different tectonic environments established that erupted lavas and their crystal cargo generally represent mixtures of discrete magma batches that experienced complex magmatic processes (e.g., Passmore et al. 2012; Bennett et al. 2019; Caracciolo et al. 2020; Pan et al. 2022; Ubide et al. 2022). These studies have demonstrated that the multi-stage storage and interaction between ascending mafic magmas and more evolved melts or partly solidified crystal mushes are typical mechanisms occurring in many volcanic systems (e.g., Hildreth and Wilson 2007; Cashman et al. 2017).

During the last couple of decades, diffusion chronometry has become a fundamental tool for tracking temporal information of magmatic processes preserved in the zoning record of minerals (Chakraborty and Dohmen 2022, and references therein). The diffusion clock usually starts when the crystals experience physical and/or chemical changes in the magmatic environment (resulting in chemical zonation in crystals), and timescales can be obtained by fitting the diffusive relaxation of compositional boundaries within zoned crystals at magmatic temperatures. Diffusion coefficients of various chemical components in olivine have already been established in an extensive experimental

This is the peer-reviewed, final accepted version for American Mineralogist, published by the Mineralogical Society of America.
The published version is subject to change. Cite as Authors (Year) Title. American Mineralogist, in press.
DOI: https://doi.org/10.2138/am-2023-9296. http://www.minsocam.org/

foundation (Chakraborty 2010). Thus, diffusion chronometry in olivine has been widely applied to establish a link between quantitative timescales and a series of evolutionary processes that magmas underwent in the plumbing system, such as crystal mush mobilization (e.g., Bradshaw et al. 2018; Caracciolo et al. 2021; Kahl et al., 2022), magma mixing (e.g., Kahl et al. 2015; Lynn et al. 2017; Caracciolo et al. 2023), and magma ascent (e.g., Brenna et al. 2018).

Most of these studies assumed that the "diffusion clock" stops during quenching upon eruption, i.e., assuming isothermal conditions during diffusion and, thus, a constant diffusion coefficient and closed boundary condition. However, it has been extensively demonstrated that temperature exerts a significant effect on the variation of the diffusion coefficient. Numerical simulation using MELTS suggests that the combination of growth and diffusion produces different shapes of profiles than the simple fixed boundary model and obtains significantly longer timescales (Costa 2008). The comparison with the relatively immobile diffusion elements (e.g., P in olivine, Shea et al. 2015b; Al in olivine, Newcombe et al. 2014; Mutch et al. 2019; Ba in sanidine, Chamberlain et al. 2014; Rout and Wörner 2020) could be utilized as an indicator to select the appropriate initial and boundary conditions. The decoupling of contemporaneous diffusion and growth can be further identified by binary plots of forsterite vs Ni in olivine, which exhibits an increasing linear trend modified during diffusion (e.g., Gordeychik et al. 2018). Petrone et al. (2016) proposed a non-isothermal diffusion incremental step model (NIDIS) to address complicated zone boundaries produced at different temperatures within a single crystal. Moreover, Rout et al. (2020) conducted stepwise temperature diffusion experiments to evaluate the associated errors of NIDIS and improve the accuracy. In these cases, diffusion chronometry is commonly applied to zoned crystals preserved in tephra samples since the diffusion clock stops playing a role in eruption. However, with cooling lava flows, diffusion proceeded with crystal growth in magmatic environments with decreasing temperatures. The diffusion model needs to take into account the effects that the compositional profiles are modified by moving and changing boundary conditions.

In this study, to simultaneously assess crystal growth and melt composition variation during diffusion, we employed a dynamic diffusion model with constantly adapting boundary conditions combined with the Monte Carlo simulation method to fit moving and changing boundary conditions during cooling and crystallization of the basaltic magmas. This approach was used to fit the Fe-Mg diffusion profiles in olivine crystals embedded in crystalline groundmass from the Tianchi shield-forming basalts, Changbaishan Volcanic Field (CHVF). Timescales from diffusion modelling were combined with chemical (bulk-rock and mineral geochemistry) and textural (petrography, zoning patterns of olivines) data to elucidate the storage and transport conditions of basaltic magmas under the Tianchi volcano.

DOI: https://doi.org/10.2138/am-2023-9296. http://www.minsocam.org/

GEOLOGICAL SETTING AND SAMPLING

The Changbaishan Volcanic Field (CHVF) is among the largest active intra-continental volcanic systems on Earth over the past ~28 Ma. It is located at the northern edge of the Archean-Proterozoic North China Craton (Hong et al. 2017). The CHVF comprises three mainly polygenetic volcanic edifices including Namphothe, Wangtian'e, and Tianchi volcanoes, and more than 200 monogenetic volcanic cones (Sun et al. 2017). In general, the Tianchi volcano experienced a three-stage magmatic evolution. The onset of polygenetic volcanism at Tianchi volcano was marked by eruptions of plateau-forming voluminous basaltic lavas in the early Miocene, followed by volumetrically smaller cone-constructing eruptions composed of mainly trachytic rocks, and catastrophic caldera-forming eruptions of more silicic magmas (predominantly comendites and pantellerites; e.g., Zhang et al. 2018). Based on field, petrographic, and geochemical evidence, these silicic magmas are proposed to be genetically related to the crustal differentiation and evolution of basaltic magmas (e.g., Iacovino et al. 2016; Andreeva et al. 2019; Lee et al. 2021).

Alkali olivine basalts and tholeiite basalts form the main part of the Tianchi shield-like basaltic lava plateau that covers an area of ~7200 km^2 (Fig. 1). K–Ar age data divide the shield-forming basalts of Tianchi volcano into three volcanic units: the Toudao (TD) unit (~5.02–2.35 Ma), the Baishan (BS) unit (~1.66–1 Ma), and the Laofangzixiaoshan (LFZ) unit (~1.17–0.75 Ma; Wei et al. 2007, 2013). Most of the 'A'ā lava flows from the TD and

DOI: https://doi.org/10.2138/am-2023-9296. http://www.minsocam.org/

BS units erupted from the central vent and extended more than 40 km in the peripheral area. Minor fissure eruptions along the Tumen and Heishihe River headwaters also fed the formation of the lava plateau. The youngest LFZ flows are mainly distributed on the northeast side of Tianchi volcano and exhibit shorter flow distances (< 20 km) and smaller volumes compared to those of the TD and BS units. The LFZ lava flows are commonly overlain by the alkali trachytes of the cone construction and/or pyroclastic products from the Millennium eruption (Wei et al. 2013).

In this study, we focused on basaltic samples from these three units, which cover almost the entire age spectrum of the shield-forming stage of the Tianchi eruptive history (Fig. 1; yellow stars). Lava flows from the TD and BS units are well exposed in the roadside outcrops at Yaoshui (42°31.5’N 128°3.5’E) and Jinjiang (41°59’N 127°33.5’ E), respectively. The outcrops vary in thickness and comprise multiple flow units. Each identified flow is approximately 2–5 m thick and consists of vesiculated crusts at the top and bottom (0.1–1 m) and a denser interior. A total of 13 lava flow samples were collected from the flow interiors. Five samples from the LFZ lava flow were collected from the outcrops at the Bailong hydroelectric station (42º24.2’N 128º6.1’E). These lava flows are substantially thinner (0.1–0.3 m) than the TD and BS units and are entirely composed of vesicular-rich lava.

METHODS

Bulk rock major and trace element compositions

Major element compositions of 11 samples from the three units were obtained using a PW4400 X-ray fluorescence spectrometer (XRF) on fused glass pellets. Trace elements were prepared as solutions and analyzed by a Perkin-Elmer ELAN 300D Inductively Coupled Plasma Mass Spectrometer (ICP-MS) (Part 1 of Appendix[1]). Both analyses were obtained at the Nanjing Hongchuang Exploration Technology Service Co., Ltd. (NHETS) laboratory in Nanjing, China. Details on analytical procedure and precision are identical to Pan et al. (2022) and reported therein.

Electron microprobe analysis (EMPA)

In-situ major and minor element analyses of minerals were conducted by a JEOL JXA-iSP100 electron probe micro-analyzer (EPMA) at the State Key Laboratory of Lunar and Planetary Sciences at the Macau University of Science and Technology. Mineral analyses were performed using a 1 μm beam size, 20 nA beam current at 20 kV acceleration voltage (Part 2 of Appendix[1]). The peaks of Ti and Al were counted for 30 s, and other elements for 15 s. Na and Si were measured first to minimize migration and drift. Background counting times were half of the ones on the peaks for elements, and the ZAF method was used for quantification and correction. Repeated analyses on multiple standard samples before multiple thin sections ensured the analytical precision of detected elements in the order of 1–5% relative to standard reference samples provided by the National Technical Committee for Standardization of Microbeam Analysis (China) or produced by SPI Supplies (USA). Compositional profiles of 49 olivines were measured with a step size ranging from 5 μm to 7 μm depending on grain size (Part 3 of Appendix[1]).

Electron backscatter diffraction (EBSD)

Crystal orientation is critical for diffusion modelling due to strongly anisotropic Fe–Mg diffusion in olivine (Chakraborty 2010). The crystallographic orientation of each olivine grain was determined using electron backscatter diffraction (EBSD) on a Quanta 450 scanning electron microscope at the Institute of Geology, Chinese Academy of Geological Sciences. EBSD maps over crystal areas were acquired using an acceleration voltage of 20 kV, a probe current of 1.1 nA, and a spot size of 5 μm, with step size varying from 10 to 20 μm depending on grain sizes. Measured Euler angles were converted into trends and plunges of the olivine crystallographic a-, b-, and c-axes using the Stereo32 software developed at the Ruhr-Universität Bochum (Germany). Subsequently, the angles α, β, and γ between the measured compositional profiles and the crystallographic axis orientations were calculated (Part 4 of Appendix[1]).

Thermometers and thermodynamic modelling (rhyolite-MELTS)

The crystallization temperatures of olivine cores were estimated by the Al-in-olivine thermometer (Coogan et al. 2014) using chemical compositions of Cr-spinel inclusions hosted in olivine cores and their adjacent olivine zones. The Cr# [molar Cr/(Cr+Al)] of the Cr-spinel inclusions ranges from 0.19 to 0.51, thus fitting the experimental calibration range of the thermometer (Cr#<0.69). Besides, the clinopyroxene-only thermometer (Eq. 32dH from Wang et al. 2021, which yields ±37 °C uncertainties in estimated temperature) was used to estimate the crystallization temperature of clinopyroxene microlites in the groundmass. We assumed 1 wt % of H_2O in the melt which is based on the maximum water contents obtained from Ol-hosted melt inclusions (Fo_{75-80}) in the Tianchi mafic melts (Andreeva et al. 2019).

The stability of major mineral phases in basaltic systems under various conditions was further constrained through phase equilibria modelling using rhyolite-MELTS (Gualda et al. 2012). For modelling, the bulk-rock compositions with the highest Mg# values for each unit were used as starting compositions. Compositional variations due to the initial fractionation of olivines have been removed by adding a certain amount of olivines (using Petrolog3 of Danyushevsky and Plechov 2011, Part 5 of Appendix[1]) until the melt compositions are in Fe-Mg equilibrium with the most primitive olivines found in the three units. The modelled dissolved water content in the melts was fixed at 1 wt%. The modelled redox conditions range from the Ni–NiO buffer equilibrium (NNO) to NNO-1, representing typical fO_2 values for intraplate basaltic magma (e.g., Hawai‘i and Mt. Etna volcanoes; Rowe et al. 2009), and cover the fO_2 range of open-system Tianchi magmatic processes from depth to the surface (e.g., Guo et al. 2015; Andreeva et al. 2019). The maximum pressure (8 kbar) was chosen for modelling according to the depth of the deepest magmatic reservoir estimated based on seismic tomography and magnetotelluric inversion (e.g., Ri et al. 2016; Kim et al. 2017).

RESULTS

Petrography

The petrographic observations for the three units are summarized in Table 1. Samples collected from the three units are all porphyritic in texture. Macrocrysts are set in a cryptocrystalline to highly crystalline groundmass including microlites of intergranular plagioclase (Pl), olivine (Ol), clinopyroxene (Cpx), and needle-like opaque minerals consisting of magnetite and ilmenite. Differences among the samples from the three units are mainly reflected by varying macrocryst assemblages, modes of macrocrysts, and amounts of vesicules (Table 1).

The TD basalts are slightly vesicular (~5 vol.%), containing ~10–15 vol.% macrocrysts (> 200 μm) including olivine + plagioclase + orthopyroxene (Opx; Fig. S1a) and sporadic glomerocrysts. Tabular plagioclase is the principal macrocryst phase with crystal sizes ranging from 0.2 to 2.7 mm. Euhedral olivines occur as both macrocrysts and glomerocrysts with plagioclases (Fig. S1b). Olivine macrocrysts and glomerocrysts are 0.3–0.9 mm in size and contain spinel inclusions in the cores (Fig. 2). Skeletal olivine microlites (100–200 μm) are also found (Fig. S1c). Rare orthopyroxenes only occur in polymineralic Opx-Pl glomerocrysts with bulk sizes up to 3.5 mm in diameter and exhibit

DOI: https://doi.org/10.2138/am-2023-9296. http://www.minsocam.org/

normal zoning on back-scattered electron (BSE) images (Fig. S1d).

The BS basalts contain comparable vesicule and macrocryst proportions but a different assemblage (only Ol + Pl) compared to the TD basalts (Fig. S2a). Macrocrysts are predominantly euhedral to tabular plagioclase (up to ~3 mm in length) and exhibit coarse sieve textures. Subordinated olivine is the only mafic macrocryst phase. Olivine macrocrysts are euhedral to rounded, vary in size (0.4–1.6 mm), often contain spinel inclusions in the cores, and display resorbed/embayed textures at the rims (Fig. S2b). Two types of glomerocrysts are present including Ol-Pl glomerocrysts (Fig. S2c) and sporadic olivine clusters (Fig. S2d).

The LFZ basalts are more vesicular (~10–45 vol.%) and have varying macrocryst fractions ranging from nearly aphyric basalts (<5 vol.%; Fig. S3a) to around 25 vol.% porphyritic basalts (Fig. S3b). Macrocrysts include dominant plagioclases followed by olivines. Tabular plagioclase macrocrysts (0.5–3.3 mm) display coarse sieve textures and usually contain olivine inclusions (Fig. S3c). Euhedral olivine macrocrysts are smaller (0.2–0.6 μm) than those in the TD and BS basalts. The glomerocrysts comprise coarse-grained plagioclases, which occur as a framework, and euhedral to subhedral olivines as interstitial phases (Fig. S3d). Skeletal olivine microlites can be found in the vesicular-rich samples.

Olivine chemistry and zoning

The macrocryst core compositions of TD and BS units can divided into two populations. Olivine macrocryst and glomerocryst cores with primitive compositions (High-Fo population) are in the range of $Fo_{76.8-80.1}$ [Fo = molar 100×Mg/(Mg+Fe)] for TD and $Fo_{76.2-80.0}$ for BS, respectively (Fig. 3). Olivine macrocryst cores also display relatively evolved core compositions (Low-Fo population) in the range of $Fo_{72\ -74.2}$ for TD and $Fo_{72.7-74.4}$ for BS, respectively. Both high- and low-Fo olivine populations generally exhibit normal compositional zoning with a wide core overgrown by a relatively narrow rim (Figs. 2b, 2c, and 2e). High-Fo population exhibit rim compositions in the range of $Fo_{69.8-73.5}$ for TD and $Fo_{68.3-73.7}$ for BS, and Low-Fo population have more evolved rim compositions in the range of $Fo_{67.5-70.3}$ for the TD and $Fo_{68.9-69.8}$ for the BS unit, respectively. Minor olivines of the high-Fo population from the TD (n = 6) and BS (n = 2) units display 'shoulder' type compositional zonation, which is characterized by a mostly reversely zoned interior overgrown by a normally zoned outermost rim (Figs. 2a). The LFZ unit only contains olivines with population primitive core compositions in the range of $Fo_{76.9-79.9}$. These olivines are normally zoned with rim compositions in the range of $Fo_{69.2-73.3}$. Skeletal olivine microlite cores preserve the most primitive compositions of the three units in the range of $Fo_{80.0-82.4}$ for TD, $Fo_{79.3-81.7}$ for BS, and $Fo_{79.0-79.9}$ for LFZ unit (Figs. 2d, 2f and 3). The Fo contents of most olivines decrease sharply to about Fo_{50-70} in the outermost 5–20 μm which can be identified as the distinct bright rim on the BSE images (Fig. 2). Microlites in the groundmass have the most evolved compositions of

$Fo_{66.2\text{-}69.9}$ for TD, $Fo_{68.9\text{-}69.8}$ for BS, and $Fo_{67.9\text{-}71.7}$ for LFZ, respectively.

The Mg–Fe equilibrium between olivine and bulk rock was tested using the modal of Roeder and Emslie (1970) and bulk rock Mg# [molar 100×Mg/(Mg +Fe)] is calculated assuming $Fe^{3+}/Fe^{T} = 0.1$. We found that most olivine cores and mantles (~87%) from the high-Fo population are out of equilibrium with the melt (proxied by the bulk rock) and are plotted above the equilibrium fields (Fig. 3d). Olivine cores from the low-Fo population and rims from the high-Fo population are plotted within or slightly below the equilibrium fields. Olivine rims from the low-Fo population are far below the equilibrium field.

Pyroxene and plagioclase chemistry

Compositions of orthopyroxene cores and rims in glomerocrysts from the TD unit fall in the narrow range of wollastonite $(Wo)_{2.6\text{-}3.1}$–enstatite $(En)_{78.9\text{-}79.5}$–ferrosilite $(Fs)_{17.5\text{-}18.1}$, Mg#= 81.2–81.8 and $Wo_{3.6\text{-}3.8}$–$En_{71.4\text{-}72}$–$Fs_{24.3\text{-}24.9}$, Mg#= 74–74.6, respectively.

Clinopyroxene microlites in the groundmass exhibit a relatively broad compositional range corresponding to augite and diopside, with $Wo_{42.4\text{-}47.2}$–$En_{32.8\text{-}40.2}$–$Fs_{15.7\text{-}20.9}$, Mg#= 61.9–71.6 for TD, $Wo_{40.7\text{-}46}$–$En_{34.6\text{-}41.6}$–$Fs_{15.3\text{-}20.4}$, Mg#= 62.7–72.8 for BS, and $Wo_{41.1\text{-}45.6}$–$En_{36.3\text{-}43.3}$–$Fs_{14.8\text{-}19.8}$, Mg#= 64.4–73.4 for LFZ, respectively (Figs. 4a and 4b).

Most plagioclases exhibit normal zoning patterns. Macrocryst plagioclase cores and rims from the three units have comparable anorthite contents [An = molar 100 Ca / (Ca +Na + K)] ranging from $An_{73.0-78.6}$–$An_{68.1-74.4}$ for TD, $An_{73.3-79.4}$–$An_{68.8-73.4}$ for BS, and $An_{74.0-78.4}$–$An_{69.1-73.4}$ for LFZ, respectively and belong to labradorite and bytownite (Fig. 4c). Microlite plagioclase grains in the groundmass have similar or slightly lower An contents ($An_{52.1-72.9}$ for TD, $An_{57-71.7}$ for BS, and $An_{48.4-72.4}$ for LFZ unit, respectively) compared to the macrocryst rims.

Bulk rock major and trace elements

According to the classification of Le Bas et al. (1986), the TA contents (Na_2O+K_2O wt%) of the TD unit are in the range of 3.8–4.4 wt% and belong to the sub alkaline series, whereas those for both BS and LFZ units are > 5 wt%, classifying the latter as alkaline series (Fig. 5a). Furthermore, bulk rock Mg# and MgO of the TD samples are relatively high (49.2–50.6; 6.0–6.5 wt%) in comparison to the BS (47.5–49.1; 5.1–5.6 wt%) and the LFZ (47.1–48.4; 4.7–5.3 wt%) samples. MgO correlates negatively with SiO_2, TiO_2, Na_2O, K_2O, Al_2O_3, and P_2O_5, and positively with FeO_T, MnO, CaO, Ni, and Cr (Figs. 5 and S4). Correlations between oxides are consistent with the established evolution trend of the literature dataset of the CHVF basaltic samples compiled by Zhang et al. (2018).

On primitive mantle-normalized trace element diagrams and chondrite-normalized rare earth element (REE) diagrams (Fig. S5), samples from the TD unit exhibit patterns resembling enriched mid-ocean ridge basalts (E-MORB), while samples from the BS and LFZ units display patterns similar to ocean island basalts (OIB).

Magma storage conditions

The observed high diversity of mineral chemistry and zoning patterns indicate that the Tianchi magmatic system may have involved multiple magmatic environments for crystal stalling and recycling. Various magmatic environments could be constrained by combining thermometry and thermodynamic modelling. The crystallization temperatures estimated from the spinel inclusions at the olivine cores of the high-Fo olivine population were used to represent the magma storage temperatures at crustal reservoirs. The results return progressively decreasing average temperatures from 1201 ± 15 °C (1σ deviation) for TD, 1191 ± 17 °C for BS to 1155 ± 12 °C for LFZ (Fig. 6a). The estimated crystallization temperatures of clinopyroxene microlites in the groundmass are 1023 ± 16 °C for TD, 1059 ± 24 °C for BS, and 1059 ± 16 °C for LFZ, respectively (Fig. 6a), and correspond to temperatures during the last magma ascending stage and further cooling on the surface.

The stability of liquidus olivine was also constrained by rhyolite-MELTS modelling. A series of isobaric cooling (pressure intervals of 0.5 kbar) crystallization paths with 1 wt% bulk H_2O contents and fO_2 condition at NNO and NNO-1 were modelled with temperature steps of 1 °C. The results show that the liquidus phase assemblage is strongly pressure-dependent. The maximum P-T conditions for liquidus olivine are 1227–1237 °C and 5–5.5 kbar for the TD unit, 1222–1232 °C and 5–5.5 kbar for the BS unit, as well as 1166–1177 °C and 3.5–4 kbar for the LFZ unit over the range of considered fO_2 conditions (Figs. 6b, 6c and 6d). Accordingly, corresponding maximal crystallization depths are ~20 km for both TD and BS units, and ~15 km for the LFZ unit, assuming an average crustal density of 2.7 g/cm^3. Olivine is replaced by Opx (enstatite-rich) as the liquidus phase at deeper depths (i.e., higher pressure). Moreover, the co-existence of Ol ± Pl ± Opx under mid-crustal pressures in our modelling reconciles with the observed natural glomerocryst assemblages of the Tianchi shield-forming basalts. Besides, rhyolite-MELTS modelling also indicates that the low-Fo olivine macrocrysts in the TD and BS units start to crystallize at temperatures <1140 °C, coexisting with clinopyroxene and/or plagioclase, only if the pressures are <4 kbar for the TD unit (~15 km) and <3.5 kbar for the BS unit (~13 km).

DYNAMIC DIFFUSION MODEL WITH CONSTANTLY ADAPTING BOUNDARY CONDITIONS

Olivine macrocrysts were embedded in a crystalline groundmass in the Tianchi shield-forming basalts. These olivines are either normally zoned or 'shoulder' type zoned with more evolved rims in contact with the crystalline groundmass. This suggests that the olivine edge records the latest magmatic environments shared by all olivines, i.e., slow cooling and further crystallization within lava flows. The growth of compositionally different rims of two populations is likely a response to different magmatic processes affecting the crystal cargo, such as magma residence, magma ascent, and lava emplacement. Therefore, the timescales obtained from the olivine rims must represent the sum of both the pre-eruption history and the cooling within the lava flows. Time-related information on the above-mentioned magmatic processes is locked in the chemical profile of compositionally zoned olivines and can be retrieved through elemental diffusion chronometry. However, major obstacles in extracting timescales are how the diffusion process itself is modified by moving and changing boundaries that result from melt evolution and crystal growth (e.g., Costa 2008; Dohmen et al. 2017; Chakraborty and Dohmen 2022).

We have employed a one-dimensional dynamic Fe-Mg interdiffusion model from Couperthwaite et al. (2021) to constantly adapt variable boundary conditions induced by crystal growth and melt composition variations. This diffusion model is an iterative finite difference model and diffusion is described as a function of temperature, which is then linked to melt composition and crystal growth rate. This model has been successfully applied to a series of terrestrial (Piton de la Fournaise, La Réunion; Couperthwaite et al. 2021; 1950 AD Southwest Rift Zone eruption; Kahl et al. 2023) and lunar (lunar basalts delivered by Appolo-15; Bell et al. 2023) lava samples, and considerably advanced the fitting degree of measured olivine compositional profiles. In this contribution, we combined the dynamic Fe-Mg interdiffusion model with a Monte Carlo simulation approach to determine timescales that fit best the compositional profiles of olivine macrocrysts in the Tianchi shield-forming basalts.

Modelling approach

First, it is reasonable that the melt composition constantly evolves as crystallization proceeds during the entire cooling history, including pre-, syn- and post-eruptive processes. Hence, we can describe the change of the equilibrium Fo content of olivines with the constantly changing composition of the liquid based on the Fe-Mg partitioning coefficient between Ol and melt (e.g., Toplis 2005; Matzen et al. 2011). Consequently, the instantaneous olivine-melt boundary conditions can be constrained by the liquid line of descent (LLD) which can be determined by rhyolite-MELTS. The LLDs for the three units under NNO-1 and 1 kbar are parameterized as a function of olivine equilibrium compositions and temperature (Equation 3 in Table 2 and Fig. S6). We also assumed a one-stage linear cooling history to connect the LLD with time (Equation 6 in Table 2). The constant cooling rate (q) can be defined by three parameters: the diffusion initial temperature (T_0), the diffusion final temperature (T_{min}), and the time (t). By applying the parameterized LLD, T_0 ranges were chosen from the temperatures that correspond to the measured core and rim Fo contents of each crystal. T_{min} is thought to correspond to post-eruptive cooling temperatures within flow lavas. Hence, the T_{min} ranges for each unit are determined according to the crystallization temperature range of clinopyroxene microlites in the groundmass. Natural processes, especially volcanic crystals that recorded pre-eruption and post-eruption processes, tend to experience an exponential cooling rate instead of a linear cooling history (Zhang 2008). Nevertheless, our multiple simulations demonstrated that the dynamic diffusion models based on both cooling models generate well-fitting and comparable timescale results. This suggests that the linear assumption is still valid assuming that the establishment of profile shape in multi-stage magmatic processes is controlled by the magmatic environment of predominant magmatic events (Detailed results and discussions are shown in Fig. S7 and Part 1 of Appendix[4]). It is worth noting that the best-fit linear cooling rates for crystals that experienced complex magmatic processes do not accurately correspond to any specific magmatic event. More accurately, it indicates the predominant magmatic environment that drove the shape of the diffusion profile over multi-stage processes. The cooling rate range is limited to less than 0.013 °C/s, representing the boundary cooling rate between polyhedral and skeletal olivine (Welsch et al. 2013).

The diffusion equation of simultaneous development of Fe-Mg diffusion and growth of olivine has already been described in Equation 1 in Table 2 (Zhang 2008). Hence, in the second step, we are considering that the olivine-melt boundary could move towards the surrounding melts due to the growth of olivine crystals. Notably, during linear cooling, olivine crystals commonly show a gradually increasing growth rate in response to decreasing temperature (e.g., Newcombe et al. 2014). We adopted a T-dependent gradually increasing growth rate (G), which is determined by the half-growth rate at G_{min}

(G_0), T_0, and T_{min} (Equation 4 in Table 2; Couperthwaite et al. 2021). The growth rate range is confined to less than 10^{-8} m/s, which represents the growth rate boundary between polyhedral and skeletal olivines (Jambon et al. 1992). By integrating the growth rate, cooling rate, and melt evolution paths and adjusting their parameters, the constantly adapting boundary conditions can be expressed as follows:

$$t = 0,\ X = X_0;\ Fo = Fo_0,$$

$$t > 0,\ X = X_0 + Gt;\ \ Fo = f(T)$$

where X_0 is the initial boundary location between the crystal and melt, and Fo_0 is the initial boundary composition of the olivine. All modelling took into account the anisotropy (Equations 5 and 8) and compositional dependence of olivine and adopted the Fe-Mg diffusivity (D) of Equation 7 in Table 2 (Dohmen and Chakraborty 2007a; 2007b). The redox condition was set at NNO-1 buffer and calculated according to Equation 9 in Table 2 (Ballhaus et al. 1991).

The model tracks the boundary compositions by adjusting the LLD via the cooling rate, which controls other variables including, growth rate, diffusivity, and absolute oxygen fugacity. To accomplish this, a hybrid Monte Carlo and finite difference approach was employed. Sample parameter values were randomly varied from specified ranges ($T_{0i},$ $T_{min},$ $q,$ G_0), with each parameter following a uniform distribution. The Forward Euler method was implemented following the logic outlined by Couperthwaite et al. (2021) and shown in the workflow chart of Fig. S8. To ensure method convergence and stability, the time step (Δt) and spatial step (Δx) adhere to the Courant–Friedrichs–Lewy condition:

$$\frac{D\Delta t}{\Delta x^2} = 0.2$$

The goodness is represented by r^2 (coefficient of determination), which measures the correlation between the computed and the measured profile and calculates as follows:

$$r^2 = 1 - \frac{\sum_{i=1}^{n}(Fo_i - \widehat{Fo_\iota})^2}{\sum_{i=1}^{n}(Fo_i - \overline{Fo_\iota})^2}$$

Where Fo_i is the measured experimental Fo content, $\overline{Fo_\iota}$ is the means of measured experimental Fo content, and $\widehat{Fo_\iota}$ is the theoretically expected Fo content. Simulations were repeated 6000 times and the optimal solution was, subsequently, selected from the resulting set of solutions. A Monte Carlo simulation was used to estimate the uncertainty related to the diffusivity of Equation 7 in Table 2. The primary variables that contribute to the olivine Fe-Mg interdiffusion coefficients include the temperature (±20 ℃), oxygen fugacity (±0.5 log units), and olivine composition (±1.7 mol % on Fo). The results indicate that uncertainties of 1σ gradually amplify with increased diffusion timescales (Fig. S9). A maximum uncertainty of ±157.4 days for the TD and BS high-Fo populations and ±41 days for the low-Fo populations. The high-Fo population of the LFZ unit indicates the maximum uncertainty of ±53.7 days.

Modelling results

We conducted the modelling on 49 olivine crystals from the three units that display core-rim zoning patterns. Two traverses within the same olivine grains were measured to check for timescale consistency along different profiles. Each traverse was oriented perpendicular to a well-established crystal face, avoiding corners to limit the effects of merging diffusion fronts (Shea et al. 2015a). We assumed the homogenous initial conditions for all olivines based on the well-defined core compositional plateaus and monotonically decreasing rim compositions (Fig. 7). Some olivines exhibit significant bright rims on the BSE images (Figs. 2c and 2e) characterized by a sharp decrease in Fo content at the exterior rims. We interpreted them as a disequilibrium growth during the late stage of lava flows and rejected these bright rims for diffusion modelling. For each traverse, the best-fitting curve was chosen based on the highest r^2 value from the 6000 modelling simulations. All of the best-fitting curves carry r^2 values higher than 0.99 and are in good agreement with the measured profiles (Fig. 7). Appendix[3] summarizes the timescale results and relevant variables (q, G_0, T_i, and T_f) of the best-fitting curves.

Kernel density estimate (KDE) distribution curves of modelled timescales and related variables are shown in Figs. 8 and S6. High-Fo populations from the TD and BS units record a large range of timescales, varying from 172.8 to 850 days and 226.7 to 786.1 days, respectively. KDE distribution curves of the TD high-Fo population show a prominent peak at 496 days and two minor peaks at 236 and 821 days (Fig. 8a). BS high-Fo population exhibits a major peak at 501 days and a minor peak at 306 days (Fig. 8b). Timescales of the low-Fo olivine populations from the TD and BS units are below 100 days. The most probable timescales (relative probability > 0.01) for the low-Fo populations are 19–55 days for the TD unit (Fig. 8a), with a main peak at 36 days, and 31–60 days for the BS unit (Fig. 8b), with a main peak at 44 days. For the LFZ unit, 80% of high-Fo population provide timescales shorter than 100 days, with a main peak in the KDE distribution at 57 days (Fig. 8c). Only five profiles (20%) record timescales longer than 100 days, with a minor peak at 130 days.

The transport of basaltic magmas in the crust mainly occurs as channeled ascent involving the movement of magma through discrete networks of narrow conduits, as frequently observed by field investigation and geophysical observations (e.g., Palma et al. 2011; Vergniolle and Métrich 2022). The minimal magma supply rate (Q_c, i.e. to impede solidification in the dikes) of the Tianchi shield-forming basalts was quantitatively evaluated by 50,000 calculations using the modified model (Eq. 1) of Menand et al. (2015) [Equation 4 of Morgado et al. (2017); details are shown in Part 2 of Appendix[4]]. Magma supply rates associated with the timescales of each crystal were calculated assuming that the ascending magmas (20 km for the TD and BS units, 15 km for the LFZ unit, the maximum olivine crystallization depth estimated via rhyolite-MELTS) were transported in a cylindrical conduit with a radius of 5 m (representative dyke model of stratovolcanoes; Gonnermann and Manga 2013). All the results are far below the modelled minimum magma supply rate (Q_c = 8.3 km^3/yr; Fig. 8d) even for the shorter timescales recorded by the TD and BS low-Fo populations (most probable magma supply rates are 0.008–0.047 km^3/yr) and the LFZ high-Fo population (0.026–0.052 km^3/yr). The shorter timescales are related to the higher cooling rates (~10^{-6}–10^{-5} °C/s) and faster G_0 (~10^{-13}–10^{-12} m/s), which is one order of magnitudes higher than those corresponding to the longer timescales recorded by the TD and BS high-Fo populations (Figs. 8e and 8f). These characteristics demonstrate the relatively cold and highly undercooling magmatic environments these crystals experienced, probably corresponding to the processes during magma ascent and subsequent crystallization within the cooling lavas (e.g., Gordeychik et al. 2018; Couperthwaite et al. 2020). In comparison, most estimated magma supply rates based on timescales obtained for TD and BS high-Fo populations are significantly below the Qc (0.0014–0.0038 km^3/yr) with lower cooling rates (~10^{-7}–10^{-6} °C/s) and slower G_0 (~10^{-14}–10^{-13} m/s). The lower G_0 and cooling rates reveal that the predominant magmatic environments where these crystals stalled and diffusion occurred are hotter and relatively adiabatic compared to that of low-Fo populations of TD and BS units, and high-Fo population of LFZ unit. The long timescales recorded by the TD and BS high-Fo populations reflect more complex magmatic processes and support the hypothesis that the magma underwent some stagnation in the shallow magmatic storage system where high-Fo olivines diffusively re-equilibrated. Thus, reported timescales correspond to the sum time including shallow storage, magma ascent, and further cooling on the surface within the lava flows.

MAGMA PLUMBING SYSTEM RECORDED BY OLIVINES

In recent times, multi-level basaltic magmatic plumbing systems have been identified for several tectonic settings. For example, petrological studies of the 1783–1784 AD Laki eruption in Iceland recognized that more primitive olivines crystallized in the mid-crust and were transferred to shallower storage levels before eruption (e.g., Passmore et al. 2012; Neave et al. 2014; Hartley et al. 2016). In a subduction-related setting, via combining petrological investigations and olivine diffusion modelling on Mt. Etna Volcano which erupted in 1669 and 1991–2008, Kahl et al. (2011, 2015, 2017) showed that the evolution of primitive magmas involved at least five different magmatic environments (MEs) and that magmas mixed and were transported over two years preceding the start of the eruption. Moreover, a recent study on Datong Volcanic Field, North China Craton concluded that open system processes involving multi-level mush disaggregation and mafic magma recharge played an important role in the textural diversity and evolution of these intra-continental tholeiites (Pan et al. 2022).

Previous petrological studies of the Tianchi basaltic system concluded that these magmas ascended directly from the deep sources to the surface without significant crustal residence (e.g., Fan et al. 2007; Lee et al. 2021). However, bulk-rock compositions exhibit relatively low Ni (< 170 ppm) and Cr (< 230 ppm) implying significant crustal differentiation processes of mantle-derived magmas prior to eruption (Figs. S4e and S4f). The magnetotelluric inversion data suggest that the high velocity regions ranging from the summit to 20 km depth underneath the Tianchi volcano represent a significant volume of the crust modified by magmatism (e.g., Choi et al. 2013; Ri et al. 2016). This zone is interpreted as a complex trans-crustal magma plumbing system with magma reservoirs located at diverse depths. Glomerocrysts from three units exhibit mineral assemblages (Ol + Pl ± Opx) similar to those predicted by rhyolite-MELTS for mid-crustal depths for the LFZ unit (~15 km) and deeper depths for the TD and BS units (~20 km), indicating that they could represent exhumed pieces of the crystal mush reservoirs. The similar Fo contents of olivines in the high-Fo macrocrysts and glomerocrysts support their common origin. The presence of homogenous core compositional plateaus (Figs. 2a, 2b, and 2e) may be attributed to a prolonged residence time in a reservoir(s) where the crystals grew under stable magmatic conditions or as a result of being re-equilibrated through diffusion at high temperatures. The sporadic reversely zoned olivines reflect interaction with magmas necessarily more primitive that are in equilibrium with the most magnesian compositions found in the TD ($Fo_{79.2\text{-}82.2}$) and BS units ($Fo_{79.2\text{-}81.5}$). This feature can be considered as a record of mafic magma recharge resulting in the overgrowth of more Fo-rich rims on olivine cores that previously crystallized in the reservoirs.

Given the long timescales, low cooling rates, and slow crystal growth rates, it is highly likely that the outermost normal zoning from the high-Fo TD and BS populations was established in a shallower storage environment. The melt that entrained the high-Fo TD and BS populations from the deeper reservoirs, subsequently, ascended along regional faults (Yu et al. 2015; Guo et al. 2018), and stalled at shallow-crustal levels. The rounded morphology of high-Fo olivine cores and the sieve texture observed in most plagioclase macrocrysts may reflect the partial dissolution caused by decompression when the entrained crystals were carried into shallower reservoirs with more evolved melt compositions prior to the onset of the diffusion. After re-equilibration with the more evolved liquid, these high-Fo cores were overgrown by more evolved rims and the diffusion clock started. The long timescales cover an extensive range from 200 days to 800 days, indicating that magmas with entrained olivine crystals were continuously extracted from the deep reservoirs and transported through the conduits to shallow reservoirs where olivine crystals accumulated (e.g., Hartley et al., 2016; Sundermeyer et al. 2020; Caracciolo et al. 2021).

The polyhedral habitus and homogenous core plateaus (Fig. 3c) of the TD and BS low-Fo olivines (~Fo_{72-74}) indicate that these crystals likely formed in a relatively undisturbed magma in equilibrium with a more evolved residual melt. We propose that these crystals crystallized from a hybrid melt that was produced by mixing between mid-crust reservoirs ascended melts and melts stored in shallow reservoirs. Rhyolite-MELTS calculations suggest that the low-Fo macrocrysts and their hosted magmas were likely stored in a shallower reservoir (below 15 km for the TD unit and below 13 km for the BS unit; Figs. 6b and 6c) and coexisted with plagioclase ± clinopyroxene. The shorter timescales, relatively fast growth rates, and high cooling rates recorded by the normal zoning patterns from the TD and BS low-Fo populations, as well as the LFZ high-Fo population indicate late-stage magma ascent in the conduits and further cooling during lava emplacements. Degassing of the melt upon ascent likely induced rapid crystal growth (e.g. clinopyroxene microlite formation) and was accompanied by diffusive re-equilibration as the melt composition changed through rapid cooling and crystallization (e.g., Guilbaud et al. 2007). At the surface, further diffusive re-equilibration occurred contemptuously with crystal growth during lava cooling until the temperature became too low and the effective diffusion clock closed. The outermost quenched rims (bright rims on the BSE images) of the olivines likely reflect the late-stage disequilibrium growth within the lava flows.

Skeletal olivine microlites exhibit the most magnesian core and the most evolved rim compositions found in the three units (Fig. 3). These skeletal crystals commonly display half-closed or closed hopper morphology (Figs. 2d and 2f) rather than regular hopper morphology (an hourglass shape with large cavities in contact with the melts; defined by Faure et al. 2003). The typical hopper morphology usually forms under non-equilibrium conditions at high cooling rates and significant undercooling (Faure et al. 2003; 2007). The overgrowth of skeletal microlites in our samples demonstrates that these crystals underwent textural ripening that resulted from temperature fluctuations over short timescales (Faure and Schiano 2004; Colin et al, 2012). The degassing-induced rapid growth further favors infilling the initial hollow space of the hopper crystal (Donaldson 1976; Welsh et al. 2013; Couperthwaite et al. 2020). The most favorable environment for the overgrowth of skeletal microlites is therefore a degassing and turbulent magma under significant undercooling, which is likely to occur during eruptions (Welsh et al. 2009). These features demonstrate that the skeletal microlites nucleated and grew prior to cooling during the eruption. We suggest that the skeletal microlites nucleated in the replenished magma batches of more mafic compositions. These magmas ascended from the deep source, injected into the shallow (TD and BS units) or mid-crust (LFZ unit) reservoirs, and did not interact extensively with the stalled melts. These microlitic cores developed a hopper morphology in the conduits during the last rapid ascent to the surface. During the eruption and within the lava flows, further textural ripening infilled the cavity of hopper crystals and formed the half-closed or closed hopper morphology.

As illustrated in Fig. 9, we suggest that the magma plumbing systems of Tianchi shield-forming basaltic magmas underwent a structural transition. The composition and timescale differences between the high-Fo and low-Fo populations suggest that the TD and BS magmas experienced multi-stage stalling and ascent. The high-Fo populations are indicative of deeper reservoir accumulation and transfer, as well as shallow reservoir storage. The low-Fo populations nucleated from the mixed melts that were stored in the shallow reservoirs and grew more evolved rims during ascent and within the lava flows. In contrast, there is only one mid-crust reservoir for the LFZ unit. The high-Fo population were accumulated in the mid-crust reservoir, followed by direct ascent to the surface without additional residence.

IMPLICATIONS

Samples studied in this work cover almost the entire age spectrum of the shield-forming stage of the Tianchi basaltic volcanism. By combining dynamic Fe-Mg diffusion modelling in olivine crystals from three eruptive units with petrological constraints, we established the temporal and spatial evolution of the basaltic magma plumbing systems beneath the Tianchi volcano. The obtained varying timescales between the units suggest that the shield-forming basaltic magmas experienced a structural transition from multi-level stalling and subsequent ascent for the TD and BS units to direct ascent from a mid-crust reservoir to the surface for the LFZ unit. The residual, early-formed, shallow plumbing system may provide potential interconnected conduits and reservoirs for the storage and the final ascent of the later LFZ magmas. Our study reconciles, together with many previous studies (e.g., Lynn et al. 2017; Wieser et al. 2019; Gleeson et al. 2020; Stock et al. 2020; Pan et al. 2022), that for an intra-continental basaltic system, hot storage conditions are typical for a steady state open-conduit system which is driven by the regular supply of fresh, hot magma resulting in the constant presence of eruptive magma.

Another highlight of our study is that the dynamic diffusion model with constantly adapting boundary conditions can significantly improve the quality of fit to the compositional profile of olivines in lava samples. The dynamic diffusion model used here has been successfully applied to other lava samples and improved the accuracy of obtained diffusion timescales (e.g., Couperthwaite et al., 2021; Bell et al., 2023; Kahl et al., 2023). Such a scenario is expected to be quite common in most volcanic systems. Consequently, this approach is rather useful in case pyroclastic rocks are lacking and only lava samples are available, e.g., to establish diffusion timescales for zoned olivine crystals that experienced a prolonged syn- and post-eruptive history.

ACKNOWLEDGMENTS

We greatly appreciate the constructive comments and suggestions from Don Baker, Ekaterina (Kate) Kiseeva, Boris N Gordeychik, and the anonymous reviewers, which significantly improved our manuscript. We thank Ziliang Jin and Lei Jin of Macau University of Science and Technology for their help with EMPA analysis. We thank Xiaomin Wang of the Key Laboratory of Deep-Earth Dynamics of the Ministry of Natural Resources, Institute of Geology, Chinese Academy of Geological Sciences for help with EBSD analysis.

FUNDING

This research has been supported by the National Natural Science Foundation of China (No: 41922012), the National Key R&D Program of China (2019YFA0708604-2), Deep-time Digital Earth" Science and Technology Leading Talents Team Funds for the Central Universities for the Frontiers Science Center for Deep-time Digital Earth, China University of Geosciences (Beijing) (Fundamental Research Funds for the Central

Universities; grant number: 2652023001). Felix Marxer acknowledges support by the Deutsche Forschungsgemeinschaft (DFG, German Research Foundation)–HO1337/47, and TH also acknowledges support by the Alexander von Humboldt Fellowship (1207058).

REFERENCES CITED

Andreeva, O.A., Andreeva, I.A., and Yarmolyuk, V.V. (2019) Effect of redox conditions on the evolution of magmas of Changbaishan Tianchi volcano, China–North Korea. Chemical Geology, 508, 225–233.

Ballhaus, C., Berry, R.F., and Green, D.H. (1991) High pressure experimental calibration of the olivine-orthopyroxene-spinel oxygen geobarometer: implications for the oxidation state of the upper mantle. Contributions to Mineralogy and Petrology, 107, 27–40.

Bell, S.K., Morgan, D.J., Joy, K.H., Pernet-Fisher, J.F., and Hartley, M.E. (2023) Determining the thermal histories of Apollo 15 mare basalts using diffusion modelling in olivine. Geochimica et Cosmochimica Acta, 357, 77–91.

Bennett, E.N., Lissenberg, C.J., and Cashman, K.V. (2019) The significance of plagioclase textures in mid-ocean ridge basalt (Gakkel Ridge, Arctic Ocean). Contributions to Mineralogy and Petrology, 174, 49.

Bradshaw, R.W., Kent, A.J.R., and Tepley, F.J. (2018) Chemical fingerprints and residence times of olivine in the 1959 Kilauea Iki eruption, Hawaii: insights into picrite formation. American Mineralogist, 103, 1812–1826.

Brenna, M., Cronin, S.J., Smith, I.E.M., Tollan, P.M.E., Scott, J.M., Prior, D.J., Bambery, K., and Ukstins, I.A. (2018) Olivine xenocryst diffusion reveals rapid monogenetic basaltic magma ascent following complex storage at Pupuke Maar, Auckland Volcanic Field, New Zealand. Earth and Planetary Science Letters, 499, 13–22.

Caracciolo, A., Bali, E., Guðfinnsson, G.H., Kahl, M., Halldórsson, S.A., Hartley, M.E., and Gunnarsson, H. (2020) Temporal evolution of magma and crystal mush storage conditions in the Bárðarbunga-Veiðivötn volcanic system, Iceland. Lithos, 352–353.

Caracciolo, A., Kahl, M., Bali, E., Guðfinnsson, G.H., Halldórsson, S.A., and Hartley, M.E. (2021) Timescales of crystal mush mobilization in the Bárðarbunga-Veiðivötn volcanic system based on olivine diffusion chronometry. American Mineralogist, 106, 1083–1096.

Caracciolo, A., Bali, E., Halldórsson, S.A., Guðfinnsson, G.H., Kahl, M., Þórðardóttir, I., Pálmadóttir, G.L., and Silvestri, V. (2023) Magma plumbing architectures and timescales of magmatic processes during historical magmatism on the Reykjanes Peninsula, Iceland. Earth and Planetary Science Letters, 621: 118378.

Cashman, V., Stephen, R., Sparks, J., and Blundy, J.D. (2017) Vertically extensive and unstable magmatic systems: a unified view of igneous processes. Science, 355, 1280.

Chakraborty, S. (2010) Diffusion coefficients in olivine, wadsleyite and ringwoodite. Reviews in Mineralogy and Geochemistry, 72, 603–639.

Chakraborty, S., and Dohmen, R. (2022) Diffusion chronometry of volcanic rocks:

looking backward and forward. Bulletin of Volcanology, 84, 57.

Chamberlain, K.J., Morgan, D.J., and Wilson, C. J. N. (2014) Timescales of mixing and mobilization in the Bishop Tuff magma body: perspectives from diffusion chronometry. Contributions to Mineralogy and Petrology, 167, 1034.

Cherniak, D.J., and Dimanov, A. (2010) Diffusion in Pyroxene, Mica and Amphibole. Reviews in Mineralogy and Geochemistry, 72, 641–690.

Choi, S., Oh, C.W., and Götze, H.J. (2013) Three-dimensional density modelling of the EGM2008 gravity field over the Mount Paekdu volcanic area. Journal of Geophysical Research: Solid Earth, 118, 3820–3836.

Colin, A., Faure, F., and Burnard, P. (2012) Timescales of convection in magma chambers below the Mid-Atlantic ridge from melt inclusions investigations. Contributions to Mineralogy and Petrology, 164, 677–691.

Coogan, L.A., Saunders, A.D., and Wilson, R.N. (2014) Aluminum-in-olivine thermometry of primitive basalts: Evidence of an anomalously hot mantle source for large igneous provinces. Chemical Geology, 68, 1–10.

Costa, F., Dohmen, R., and Chakraborty, S. (2008) Time scales of magmatic processes from modelling the zoning patterns of crystals. Reviews in Mineralogy and Geochemistry, 69, 545–594.

Couperthwaite, F.K., Thordarson, T., Morgan, D.J., Harvey, J., and Wilson, M. (2020) Diffusion timescales of magmatic processes in the Moinui lava eruption at Mauna Loa, Hawai`i, as inferred from bimodal olivine populations. Journal of Petrology, 61, egaa058.

Couperthwaite, F.K., Morgan, D.J., Pankhurst, M.J., Lee, P.D., and Day, J.M.D. (2021) Reducing epistemic and model uncertainty in ionic inter-diffusion chronology: A 3D observation and dynamic modelling approach using olivine from Piton de la Fournaise, La Réunion. American Mineralogist, 106, 481–494.

Danyushevsky, L.V., and Plechov, P. (2011) Petrolog3: Integrated software for modelling crystallization processes. Geochemistry, Geophysics, Geosystems, 12(7).

Dodson, M.H. (1973) Closure temperature in cooling geochronological and petrological systems. Contributions to Mineralogy and Petrology, 40, 259-274.

Dohmen, R., and Chakraborty, S. (2007a) Fe-Mg diffusion in olivine II: point defect chemistry, change of diffusion mechanisms and a model for calculation of diffusion coefficients in natural olivine. Physics and Chemistry of Minerals, 34, 597–598.

Dohmen, R., and Chakraborty, S. (2007b) Erratum on "Fe–Mg diffusion in olivine II: point defect chemistry, change of diffusion mechanisms and a model for calculation of diffusion coefficients in natural olivine". Physics and Chemistry of Minerals, 34, 597–598.

Dohmen, R., Faak, K., and Blundy, J.D. (2017) Chronometry and speedometry of magmatic processes using chemical diffusion in olivine, plagioclase and pyroxenes. Reviews in Mineralogy and Geochemistry, 83, 535–575.

Donaldson, C. H. (1976). An experimental investigation of olivine morphology. Contributions to Mineralogy and Petrology, 57, 187–213.

Fan, Q.C., Sui, J.L., Wang, T.H., Li, N., and Sun, Q. (2007) History of volcanic activity, magma evolution and eruptive mechanisms of the Changbai Volcanic Province. Geological Journal of China Universities (English Edition), 13, 175–190.

Faure, F., Trolliard, G., Nicollet, C., and Montel, J.M. (2003) A developmental model of olivine morphology as a function of the cooling rate and the degree of undercooling. Contributions to Mineralogy and Petrology, 145, 251–263.

Faure, F., Schiano, P., Trolliard, G., Nicollet, C., and Soulestin, B. (2007) Textural evolution of polyhedral olivine experiencing rapid cooling rates. Contributions to Mineralogy and Petrology, 153, 405–416.

Gleeson, M.L., Gibson, S.A., and Stock, M.J. (2020). Upper mantle mush zones beneath low melt flux ocean island volcanoes: insights from Isla Floreana, Galápagos. Journal of Petrology, 61, egaa094.

Gonnermann, H.M., and Manga, M. (2013) Dynamics of magma ascent in the volcanic conduit. In Modelling volcanic processes: the physics and mathematics of volcanism, p. 55–84.

Ganguly. J., and Tirone, M. (1999) Diffusion closure temperature and age of a mineral with arbitrary extent of diffusion: theoretical formulation and applications. Earth and Planetary Science Letters, 170, 131–140.

Gordeychik, B., Churikova, T., Kronz, A., Sundermeyer, C., Simakin, A., and Wörner, G. (2018) Growth of, and diffusion in, olivine in ultra-fast ascending basalt magmas from Shiveluch volcano. Scientific Report, 8, 11775.

Gualda, G.A.R., and Ghiorso, M.S. (2015) MELTS_Excel: A Microsoft Excel-based MELTS interface for research and teaching of magma properties and evolution. Geochemistry, Geophysics, Geosystems, 129, 315–324.

Guilbaud, M.N., Blake, S., Thordarson, T., and Self, S. (2007). Role of Syn-eruptive Cooling and Degassing on Textures of Lavas from the AD 1783-1784 Laki Eruption, South Iceland. Journal of Petrology, 48, 1265–1294.

Guo, W.F., Liu, J.Q., Xu, W.G., Li, W., and Lei, M. (2015) Reassessment of the magma system beneath Tianchi volcano, Changbaishan: phase equilibria constraints. Chinese Science Bulletin, 60, 3489–3500.

Guo, Z., Wang, K., Yang, Y., Tang, Y., Chen, Y.J., and Hung, S.H. (2018) The origin and mantle dynamics of Quaternary intraplate volcanism in Northeast China from joint inversion of surface wave and body wave. Journal of Geophysical Research: Solid Earth, 123, 2410–2425.

Hartley, M.E., Morgan, D.J., Maclennan, J., Edmonds, M., and Thordarson, T. (2016) Tracking timescales of short-term precursors to large basaltic fissure eruptions through Fe–Mg diffusion in olivine. Earth and Planetary Science Letters, 439, 58–70.

Hildreth, W., and Wilson, C.J. (2007) Compositional zoning of the Bishop Tuff. Journal of Petrology, 48, 951–999.

Hong, L.B., Zhang, Y.H., Xu, Y.G., Ren, Z.Y., Yan, W., Ma, Q., Ma, L., and Xie, W. (2017) Hydrous orthopyroxene-rich pyroxenite source of the Xinkailing high magnesium andesites, Western Liaoning: implications for the subduction-modified lithospheric mantle and the destruction mechanism of the North China Craton. Lithos, 282–283, 10–22.

Iacovino, K., Kim, J.S., Sisson, T., Lowenstern, J., Ri, K.H., Jang, J.N., Song, K.H., Ham, S.H., Oppenheimer, C., Hammond, J.O.S., Donovan, A., Liu, K.W., and Ryu, K.R. (2016) Quantifying gas emissions from the "Millennium Eruption" of Paektu volcano, Democratic People's Republic of Korea/China. Science Advance, 2, e1600913.

Irvine, T.N., and Baragar, W.R.A. (1971) A Guide to the Chemical Classification of the Common Volcanic Rocks. Canadian Journal of Earth Sciences, 8(5), 523–548.

Jambon, A., Lussiez, P., and Clocchiatti, R. (1992). Olivine growth rates in a tholeiitic basalt: An experimental study of melt inclusions in plagioclase. Chemical Geology, 96, 277–287.

Kahl, M., Chakraborty, S., Costa, F., and Pompilio, M. (2011) Dynamic plumbing system beneath volcanoes revealed by kinetic modelling and the connection to monitoring data: An example from Mt. Etna. Earth and Planetary Science Letters, 308, 11–22.

Kahl, M., Chakraborty, S., Pompilio, M., and Costa, F. (2015) Constraints on the Nature and Evolution of the Magma Plumbing System of Mt. Etna Volcano (1991–2008) from a Combined Thermodynamic and Kinetic Modelling of the Compositional Record of Minerals. Journal of Petrology, 56, 2025–2068.

Kahl, M., Viccaro, M., Ubide, T., Morgan, D.J., and Dingwell, D.B. (2017) A branched magma feeder system during the 1669 eruption of Mt. Etna: evidence from a time integrated study of zoned olivine phenocryst populations. Journal of Petrology, 58, 443–472.

Kahl, M., Mutch, E.J.F., Maclennan, J., Morgan, D.J., Couperthwaite, F., Bali, E., Thordarson, T., Guðfinnsson, G.H., Walshaw, R., Buhre, S., van der Meer, Q.H.A., Caracciolo, A., and Askew, R.A. (2022) Deep magma mobilization years before the 2021 CE Fagradalsfjall eruption, Iceland. Geology, 51 (2): 184–188.

Kahl, M., Morgan, D.J., Thornber, C., Walshaw, R., Lynn, K.J., and Trusdell, F.A. (2023) Dynamics of magma mixing and magma mobilisation beneath Mauna Loa—insights from the 1950 AD Southwest Rift Zone eruption. Bulletin of Volcanology, 85(12), 75.

Kim, S., Tkalčić, H., and Rhie, J. (2017) Seismic constraints on magma evolution beneath Mount Baekdu (Changbai) volcano from transdimensional Bayesian inversion of ambient noise data. Journal of Geophysical Research: Solid Earth, 122, 5452–5473.

Le BAS, M.L., Maitre, R.L., Streckeisen, A., and Zanettin, B. (1986) A chemical classification of volcanic rocks based on the total alkali-silica diagram. Journal of Petrology, 27, 745–750.

Lee, S.H., Oh, C.W., Lee, Y.S., Lee, S.G., and Liu, J. (2021) Petrogenesis of the Cenozoic volcanic rocks in Baekdu volcano in northeastern Asia and the expected depth of the magma chamber based on geochemistry, mineral chemistry, and Sr-Nd-Pb isotope chemistry. Lithos, 388–389, 106080.

Lynn, K.J., Garcia, M.O., Shea, T., Costa, F., and Swanson, D.A. (2017) Timescales of mixing and storage for Keanakāko'i Tephra magmas (1500–1820 C.E.), Kīlauea Volcano, Hawai'i. Contributions to Mineralogy and Petrology, 172, 76–96.

Matzen, A.K., Baker, M.B., Beckett, J.R., and Stolper, E.M. (2011) Fe–Mg partitioning between olivine and high-magnesian melts and the nature of Hawaiian parental liquids. Journal of Petrology, 52, 1243–1263.

Menand, T., Annen, C., and de Saint Blanquat, M. (2015) Rates of magma transfer in the crust: insights into magma reservoir recharge and pluton growth. Geology, 43, 199202.

Morgado, E., Parada, M.A., Morgan, D.J., Gutiérrez, F., Castruccio, A., and Contreras, C. (2017) Transient shallow reservoirs beneath small eruptive centres: Constraints from Mg-Fe interdiffusion in olivine. Journal of Volcanology and Geothermal Research, 347, 327–336.

Mutch, E.J., Maclennan, J., Shorttle, O., Edmonds, M., and Rudge, J.F. (2019) Rapid trans crustal magma movement under Iceland. Nature Geoscience, 12, 569–574.

Neave, D.A., Maclennan, J., Hartley, M.E., Edmonds, M., and Thordarson, T. (2014) Crystal storage and transfer in basaltic systems: the Skuggafjöll eruption, Iceland. Journal of Petrology, 55, 2311–2346.

Newcombe, M.E., Fabbrizio, A., Zhang, Y., Ma, C., Le Voyer, M., Guan, Y., Eiler, J.M., Saal, A.E., and Stolper, E.M. (2014) Chemical zonation in olivine-hosted melt inclusions. Contributions to Mineralogy and Petrology, 168, 1–26.

Palma, J.L., Blake, S., and Calder, E.S. (2011) Constraints on the rates of degassing and convection in basaltic open-vent volcanoes. Geochemistry, Geophysics, Geosystem, 12, 1–25.

Pan, R.H., Hou, T., Wang, X.D., Encarnación, J., and Botcharnikov, R. (2022) Multiple magma storage regions and open system processes revealed by chemistry and textures of the Datong tholeiitic lavas, North China Craton. Journal of Petrology, 63, egac034.

Passmore, E., Maclennan, J., Fitton, G., and Thordarson, T. (2012) Mush disaggregation in basaltic magma chambers: evidence from the AD 1783 Laki eruption. Journal of Petrology, 53, 2593–2623.

Petrone, C.M., Bugatti, G., Braschi, E., and Tommasini, S. (2016) Pre-eruptive magmatic processes re-timed using a non-isothermal approach to magma chamber dynamics. Nature Communications, 7, 12946.

Roeder, P.L., and Emslie, R.F. (1970) Olivine-liquid equilibrium. Contributions to Mineralogy and Petrology, 29, 275–289.

Ri, K.S., Hammond, J.O.S., Ko, C.N., Kim, H., Yun, Y.G., Pak, G.J., Ri, C.S., Oppenheimer, C., Liu, K.W., Iacovino, K., and Ryu, K.R. (2016) Evidence for partial melt in the crust beneath Mt. Paektu (Changbaishan), Democratic People's Republic of Korea and China. Science Advances, 2, e1501513.

Rowe, M.C., Kent, A.J., and Nielsen, R.L. (2009) Subduction influence on oxygen fugacity and trace and volatile elements in basalts across the Cascade Volcanic Arc. Journal of Petrology, 50, 61–91.

Rout, S.S., and Wörner, G. (2020) Constraints on the pre-eruptive magmatic history of the Quaternary Laacher See volcano (Germany). Contributions to Mineralogy and Petrology, 175, 73.

Rout, S.S., Schmidt, B., and Wörner, G. (2020) Constraints on non-isothermal diffusion modelling: An experimental analysis and error assessment using halogen diffusion in melts. American Mineralogist, 105, 227–238.

Shea, T., Costa, F., Krimer, D., and Hammer, J.E. (2015a) Accuracy of timescales retrieved from diffusion modelling in olivine: A 3D perspective. American Mineralogist, 100(10), 2026–2042.

Shea, T., Lynn, K.J., and Garcia, M.O. (2015b) Cracking the olivine zoning code: Distinguishing between crystal growth and diffusion. Geology, 43(10), 935–938.

Stock, M.J., Geist, D., Neave, D.A., Gleeson, M.L., Bernard, B., Howard, K.A., Buisman, I., and Maclennan, J. (2020). Cryptic evolved melts beneath monotonous basaltic shield volcanoes in the Galápagos Archipelago. Nature communications, 11, 1–13.

Sun, C., Liu, J., You, H., and Nemeth, K. (2017) Tephrostratigraphy of Changbaishan volcano, Northeast China, since the mid-Holocene. Quaternary Science Reviews, 177, 104–119.

Sundermeyer, C., Muro, A.D., Gordeychik, B., and Wörner, G. (2020) Timescales of magmatic processes during the eruptive cycle 2014–2015 at Piton de la Fournaise, La Réunion, obtained from Mg–Fe diffusion modelling in olivine. Contributions to Mineralogy and Petrology, 175, 1.

Toplis, M.J. (2005) The thermodynamics of iron and magnesium partitioning between olivine and liquid: criteria for assessing and predicting equilibrium in natural and experimental systems. Contributions to Mineralogy and Petrology, 149, 22–39.

Ubide, T., Larrea, P., Becerril, L., and Galé, C. (2022) Volcanic plumbing filters on ocean-island basalt geochemistry. Geology, 50, 26–31.

Vergniolle, S., and Métrich, N. (2022) An interpretative view of open-vent volcanoes. Bulletin of Volcanology, 84, 9.

Wang, X.D., Hou, T., Wang, M., Zhang, C., Zhang, Z.C., Pan, R.H., Marxer, F., and Zhang, H.L. (2021) A new clinopyroxene thermobarometer for mafic to intermediate magmatic systems. European Journal of Mineralogy, 33, 621–637.

Wei, H., Wang, Y., Jin, J., Gao, L., Yun, S.H., and Jin, B. (2007) Timescale and evolution of the intracontinental Tianchi volcanic shield and ignimbrite-forming eruption, Changbaishan. Northeast China. Lithos, 96, 315–324.

Wei, H., Liu, G., and Gill, J. (2013) Review of eruptive activity at Tianchi volcano, Changbaishan, Northeast China: implications for possible future eruptions. Bulletin of Volcanology, 75, 1–14.

Welsch, B., Faure, F., Bach'elery, P., and Famin, V. (2009). Microcrysts record transient convection at Piton de la Fournaise volcano (La Reunion hotspot). Journal of Petrology, 50, 2287–2305.

Welsch, B., Faure, F., Famin, V., Baronnet, A., and Bachelery, P. (2013) Dendritic crystallization: A single process for all the textures of olivine in basalts? Journal of Petrology, 54(3), 539–574.

Wieser, P.E., Edmonds, M., Maclennan, J., Jenner, F.E. and Kunz, B.E. (2019). Crystal scavenging from mush piles recorded by melt inclusions. Nature Communications, 10, 1–11.

Yu, Z., Zhang, P., Min, W., Wei, Q., Wang, L., Zhao, B., Liu, S., and Kang, J. (2015) Late Cenozoic deformation of the Da'an-Dedu Fault Zone and its implications for the earthquake activities in the Songliao basin. NE China. Journal of Asian Earth Sciences, 107, 83–95.

Zhang, Y. (2008) Geochemical kinetics. Princeton University Press, Princeton.

Zhang, M., Guo, Z., Liu, J., Liu, G., Zhang, L., Lei, M., Zhao, W., Ma, L., Sepe, V., and Ventura, G. (2018) The intraplate Changbaishan volcanic field (China/North Korea): A review on eruptive history, magma genesis, geodynamic significance, recent dynamics and potential hazards. Earth-Science Reviews, 187, 19–52.

LIST OF TABLES AND FIGURE CAPTIONS

TABLES

TABLE 1. Summary of petrographic observations for the TD, BS, and LFZ units.

TABLE 2. Summary of relevant equations and logical order in dynamic diffusion model.

FIGURES

FIGURE 1. Sketch map showing the distribution of Late Cenozoic volcanoes in the CHVF [modified from Zhang et al. (2018)]. Red circles represent the three major composite edifices (Namphothe, Wangtian'e, and Tianchi volcanoes).

FIGURE 2. BSE images highlighting the morphology and zonation characteristics of olivine macrocrysts and skeletal microlites from the TD, BS, and LFZ units. **(a)** BSE image showing shoulder zonation (normally zoned rim and reversely zoned core) of a high-Fo olivine macrocryst from the TD unit. **(b)** BSE image illustrating the normal zonation of a high-Fo olivine macrocryst from the BS unit. **(c)** BSE image illustrating the normal zonation of a low-Fo olivine macrocryst from the TD unit. **(d)** BSE image showing the skeletal olivine microlite from the BS unit. **(e)** BSE image showing the normal zonation of a high-Fo olivine macrocryst in glomerocrysts from the LFZ unit. **(f)** BSE image showing the skeletal olivine microlite in the vesicle-rich basalts from the LFZ unit. Abbreviations: Ol = Olivine, Pl = Plagioclase, Sp = Spinel, MI =Melt Inclusion.

FIGURE 3. Histograms of forsterite contents (Fo) for the Tianchi shield-forming olivine populations from the TD **(a)**, BS **(b)**, and LFZ **(c)** units. SOM: Core compositions of skeletal olivine microlites. **(d)** Rhodes diagram to test for olivine-melt equilibrium. The melt compositions are proxied by the bulk rock. The high-Fo population cores and rims have Fo contents too primitive to be equilibrium with the host melt, whereas the low-Fo population cores and high-Fo population rims are plotted within or slightly below the equilibrium field. The low-Fo population rims have Fo contents far below the equilibrium field.

FIGURE 4. Pyroxene and plagioclase endmembers, Mg# variations, and An variations diagrams for the TD, BS, and LFZ units. **(a)** Pyroxene Wo-En-Fs ternary diagram. **(b)** Pyroxene Mg# variations diagrams. **(c)** Plagioclase An variations diagrams.

FIGURE 5. (a) Na_2O + K_2O plotted against SiO_2 (TAS-diagram; Le Bas et al. 1986) for the TD, BS, and LFZ units. The alkaline-subalkaline boundary line is drawn after Irvine and Baragar (1971). **(b-f)** Representative variation diagrams (in wt%) of oxides plotted against MgO contents. Black arrows indicate expected variation trends for liquid differentiation by fractionating 10% of different major phases observed in our samples. The partition coefficients between the minerals and melts are based on the olivine–melt equilibrium model of Beattie (1993), the plagioclase–melt equilibrium model of Ariskin et al. (1993), and the clinopyroxene–melt equilibrium model of Ariskin et al. (1986). Blue arrows indicate the expected variation trends for liquid compositions by fractionating 10% based on the Rhyolite-MELTS. The model was conducted using the corrected composition of TD-2, selecting the crystallization phases including Ol+Pl+Cpx+Fe-Ti oxides, and running at 1 kbar and NNO-1 buffer. In most cases, the expected variation trends of Rhyolite-MELTS are similar to those of Ol. The shaded areas represent the published data of CHVF basaltic samples collected from Zhang et al. (2018) and references therein. Red arrows indicate the observed evolution trend of the literature dataset of Zhang et al. (2018).

FIGURE 6. **(a)** Crystallization temperature variations of olivine macrocrysts and clinopyroxene microlites from the TD, BS, and LFZ units estimated via the Aluminum-in-olivine thermometer (Coogan et al. 2014) and the Clinopyroxene-only thermometer (Wang et al. 2021). The black circles and black diamonds represent averages of temperature ranges. Rhyolite-MELTS-derived phase diagrams showing modelled liquidus phases for a bulk H_2O content of 1 wt% at NNO and NNO-1 for the TD **(b)**, BS **(c)**, and LFZ units **(d)**. Nodes represent the liquidus phase where the rhyolite-MELTS model was run for the given temperature, pressure, and oxygen fugacity. The modelled stability field of low-Fo population cores of the TD and BS units are shown in blue shades (NNO) and green shades (NNO-1).

FIGURE 7. Representative BSE images, compositional profiles, and the model best-fit curves of studied olivines. Olivine types are the normally zoned high-Fo olivine macrocryst from the TD unit **(a)**, the ‘shoulder’ type high-Fo olivine macrocryst from the BS unit **(b)**, the normally zoned low-Fo olivine macrocryst from the TD unit **(c)**, and the normally zoned high-Fo olivine glomerocryst from the LFZ unit **(d)**. BSE images and stereographic plots illustrate the location of the analytical traverses and orientation of the crystallographic axes. Red lines show best-fit curves from the dynamic diffusion model. Black dash lines indicate the assumed initial conditions. The analytical error of EPMA data is 2σ (± 0.34 mol %) in Fo contents.

FIGURE 8. Kernel density estimate plots for the TD **(a)** and BS **(b)** timescales with bandwidth 10 for the high-Fo olivines and 20 for the low-Fo olivines. Kernel density estimate plots of the LFZ **(c)** timescales with bandwidth 10. **(d)** Kernel density estimate plots showing magma supply rates with bandwidth 0.0002 for the TD and BS high-Fo olivines, and bandwidth 0.002 for the TD and BS low-Fo olivines and LFZ high-Fo olivines. The green dotted line represents the calculated minimum magma supply rate. **(e)** Kernel density estimate plots showing cooling rates with bandwidth 4×10^{-7} for the TD and BS high-Fo olivines, and bandwidth 4×10^{-6} for the TD and BS low-Fo olivines and LFZ high-Fo olivines. **(f)** Kernel density estimate plots showing G_0 with bandwidth 3×10^{-12} for the TD and BS high-Fo olivines, and bandwidth 3×10^{-11} for the TD and BS low-Fo olivines and LFZ high-Fo olivines. The colored dashed lines show the growth rate averages obtained or used in dynamic diffusion modeling based on the constant (lunar basalts delivered by Appolo-15, 2×10^{-11} m/s; Bell et al. 2023) or gradually increasing (Piton de la Fournaise, 1.9×10^{-11} m/s; Couperthwaite et al. 2021; 1950 AD Southwest Rift Zone eruption, 3.3×10^{-11} m/s; Kahl et al. 2023) growth rate models.

FIGURE 9. Schematic cartoon representing cross sections of the Tianchi magmatic system, depicting the inferred multi-level crustal plumbing system (**a**; not to scale). Mantle-derived parental magma of the TD and BS units experienced at least two stages of stalling and ascent which include a deeper magma reservoir (~20 km; **b** and **c**) and a shallower reservoir (~15 km for TD and ~13 km for BS unit; **d**). Conversely, more

evolved magmas from the LFZ unit directly ascended from mid-crust reservoirs (~15 km) to the surface without significant crustal residence **(e)**. For the TD and BS units, high-Fo olivines crystalized and accumulated in the deeper magma reservoirs. Partially reversely zoned olivine crystals recorded episodic magma recharging of more mafic magmas from deeper sources. Glomerocrysts suggest that Ol + Pl ± Opx are likely the stable mineral assemblages in the deeper reservoirs. Subsequently, residual melts were extracted from the deep reservoirs and transported to shallower levels along regional faults. Here, high-Fo olivines acquired more evolved rims, and the low-Fo olivines nucleated after the magma mixing. The melt degassed and Ol + Pl + Cpx microlites crystallized during final ascent and upon emplacement at the surface. All zoned olivines diffusively equilibrated until the lava flow sufficiently cooled. For the LFZ unit, high-Fo olivines and plagioclases are the stable mineral assemblages in the mid-crust reservoirs. High-Fo olivines acquired more evolved rims and diffusional equilibration occurred during ascent and within the lava flows, without significant crustal residence.

APPENDIX TEXT

Appendix[2]: Supplementary Figures

FIGURE S1. Petrographic photos of TD basalts. (**a**) Cross-polarized light (XPL) image showing plagioclase and olivine macrocrysts in a fine-grained groundmass. (**b**) XPL image showing a glomerocryst containing tabular plagioclases and embedded euhedral olivine. Plagioclase cores display sieve texture. (**c**) XPL image showing a skeletal olivine microlite in a fine-grained groundmass. (**d**) Backscattered electron (BSE) image displaying a cm-sized glomerocryst including tabular plagioclases and euhedral orthopyroxenes. Orthopyroxenes are normally zoned. Orthopyroxene cores are in contact with plagioclases in the glomerocrysts but are isolated by orthopyroxene rims from the groundmass. Abbreviations: Ol = Olivine, Pl = Plagioclase, Opx = Orthopyroxene.

FIGURE S2. Petrographic photos of BS basalts. (**a**) XPL image illustrating plagioclases and olivine macrocrysts in a fine-grained groundmass. (**b**) XPL image showing the resorbed/embayed rims of the olivine macrocryst. (**c**) XPL image showing a glomerocryst containing subhedral olivines and tabular plagioclase. (**d**) XPL image exhibiting a glomerocryst consisting of olivines. Abbreviations are as in Fig. S1.

FIGURE S3. Petrographic photos of LFZ basalts. (**a**) XPL image illustrating nearly aphyric basalts including abundant vesicles. Skeletal olivine microlites are also found in these vesicle-rich basalts. (**b**) XPL image showing high crystallinity basalts containing plagioclase macrocrysts and polymineralic glomerocrysts composed of olivines and plagioclases. The plagioclases usually form the framework of the glomerocrysts, and euhedral to subhedral olivines occur within the framework as interstitial phases. (**c**) XPL image showing a cm-sized plagioclase macrocryst containing an olivine inclusion. (**d**) XPL image illustrating a glomerocryst composed of tabular plagioclase and subhedral olivine set in a coarse-grained groundmass. Plagioclase and olivine in glomerocrysts display similar sizes and the plagioclase cores display sieve texture. Abbreviations are as in Fig. S1.

FIGURE S4. Variation diagrams of major elements (in wt%) and trace elements (in ppm) plotted against MgO contents (in wt%) for the TD, BS, and LFZ bulk-rock compositions. Black arrows indicate expected variation trends for liquid differentiation by fractionating 10% of different major phases observed in our samples. The colored arrows and shaded areas are the same as in **Fig. 5**.

FIGURE S5. Primitive mantle normalized trace elements patterns (a) and chondrite normalized REE patterns (b) for the TD, BS, and LFZ units. The trace element data of N-type MORB are from Saunders and Tarney (1984) and Sun (1980), and the REE data are from Sun and McDonough (1989). The data for E-type MORB are from Klein (2003). The data for OIB and primitive mantle and C1 chondrite normalizing values are from Sun and McDonough (1989).

FIGURE S6. Melt evolutionary paths of olivine equilibrium composition over the temperature range 1250–850 °C for the TD, BS, and LFZ units modelled using rhyolite-MELTS. All models were conducted under 1 kbar and NNO-1 buffer. The colored lines in **(b, c, d)** represent the T_0 and T_{min} based on the Kernel density estimate with bandwidth 7. The results show that high-Fo populations from the TD and BS units record a large range of T_0, varying from 1128 to 1193 ℃ and 1139 to 1197 °C, respectively. T_{min} from the high-Fo populations (peak at 1100 °C of the TD unit and 1094 °C of the BS unit) is similar to or slightly lower than T_0 of the low-Fo populations (peak at 1100 °C of the TD unit and 1108 °C of the BS unit) at the same unit. T_{min} from the low-Fo populations show a prominent peak at 1083 °C for the TD unit and 1084 °C for the BS unit. T_0 and T_{min} from the high-Fo population of the LFZ unit display a significant peak at 1130 °C and 1189 °C, respectively.

FIGURE S7. Representative BSE images, compositional profiles, and the model best-fit curves of high-Fo populations from the TD and BS units based on the linear cooling (**a and c**) and exponential cooling (**b and d**) models. BSE images and stereographic plots illustrate the location of the analytical traverses and orientation of the crystallographic axes. Red lines show best-fit curves from the dynamic diffusion model. Black dash lines indicate the assumed initial conditions. The analytical error of EPMA data is 2σ (± 0.34 mol %) in Fo contents. The results suggest that both cooling models generate well-fitting and comparable timescale results.

FIGURE S8. Schematic diagram showing the workflow of the dynamic diffusion model (modified from Couperthwaite et al. 2021 and Bell et al. 2023).

FIGURE S9. A binary graph showing the obtained timescales and their 1σ uncertainty.

This is the peer-reviewed, final accepted version for American Mineralogist, published by the Mineralogical Society of America.
The published version is subject to change. Cite as Authors (Year) Title. American Mineralogist, in press.
DOI: https://doi.org/10.2138/am-2023-9296. http://www.minsocam.org/

The variables that control the diffusivity related uncertainties include the temperature (±20 °C), oxygen fugacity (±0.5 log units), and olivine composition (±1.7 mol % on Fo). The modelled results indicate that uncertainties gradually amplify with increased diffusion timescales.

FIGURE S10. The expected range of critical magma supply rates via Monte Carlo simulations. The minimum magma supply rate (Q_c) is 8.3 km^3/yr.

Appendix[4]: Supplementary remarks

Part 1: Comparison of dynamic diffusion model based on linear cooling and exponential cooling models

The olivine crystals in our study, especially high-Fo populations of TD and BS units, recorded a series of magmatic events such as shallow storage, magma ascent, and lava emplacement. The cooling rates of magmatic environments are varying in different stages. T This implies that it is necessary to verify the reliability of using a simple linear cooling model for crystals undergoing complex magmatic processes. Zhang (2008) suggests that the exponential cooling model is more suitable for the cooling history of volcanic systems that underwent pre-eruption and post-eruption processes:

$$T = T_{min} + \frac{T_0 - T_{min}}{1 + \frac{t}{\tau}}$$

The τ is the time when the temperature is 1-1/e of the T_0. This equation depicts a cooling process in which the cooling rate grows exponentially as the temperature declines. We separately applied the linear and exponential cooling models to the representative compositional profiles of high Fo-olivines from each thin section in the TD and BS units (n =11) while keeping the other variables constant. The results show that both cooling models can fit the composition profile well (Fig. S7) and that adjustments in the cooling model have no significant effect on the results of the timescale and other variables (Table S1). This demonstrates that although the exponential model aligns with the cooling history of volcanic systems, a simple linear model is as effective. We consider that the following two reasons can explain why the linear modal is still well-fitted:

1. The range of temperature variation is small, and a linear model can be regarded as an approximation of exponential models. We rejected this hypothesis as our simulations showed that both the linear and exponential models produced significant temperature ranges (Table S1). Geothermometer constraints based on high-Fo olivine cores and clinopyroxene microlites indicate that magma experienced significant cooling from sub-surface magma reservoirs to lava flows (Fig. 6).
2. In multi-stage magmatic processes of Tianchi basaltic magma systems, the establishment of compositional profile shape is controlled by the magmatic environment of predominant magmatic events, and the modification by the subordinate magmatic environments on profile shape can be moderately ignored. The magma temperature and crystal residence timescale govern the extent to profile shape is modified by diffusion. Petrone et al. (2016) proposed a non-isothermal diffusion

incremental step model (NIDIS) to solve the multi-stage diffusion question. In their samples, clinopyroxene crystals in tephra recorded the two-stage processes before the eruption. The high temperature and significant crystal residence timescales in the second stage indicate that the diffusion in the second stage significantly modified the profile shape established in the first stage. However, in our samples, compared to the timescales of magma ascent and lava emplacement, the high-Fo olivines experienced significantly longer timescales and high temperatures for residence in shallow magma reservoirs. The adequate residence time and relatively high temperature in the reservoirs enable the compositional profile to primarily record the timescales and environmental information of the shallow magma reservoir. The lower cooling rates (~10^{-7}–10^{-6} °C/s) and slower G_0 (~10^{-14}–10^{-13} m/s) obtained from the high-Fo populations of the TD and BS unit (Figs. 8e and 8f) imply a hot and relatively adiabatic magmatic environment, thus support the hypothesis that the magma underwent some stagnation in the shallow magmatic storage system. In comparison, timescales of magma ascent and surface emplacement are much shorter (19–66 days obtained from low-Fo populations of the TD and BS units). The shorter timescales and lower magma temperatures make it difficult to further effectively modify the compositional profiles that have already been formed through diffusion re-equilibration in shallow magmatic reservoirs.

Our simulations demonstrated that the dynamic diffusion models based on two cooling models generate well-fitting and comparable timescale results. We still prefer to use simple linear models because they provide cooling rate information to indicate the predominant magmatic environment where the crystals were experienced. It is worth noting that the best-fit linear cooling rate for crystals that record complex magmatic processes is not representative of any specific magmatic event. More accurately, it indicates the principal magmatic environment that drove the shape of the diffusion profile over multi-stage processes. In contrast, the parameter τ provided by the exponential model represents the time when the initial temperature of the diffusion decreases to its 1-1/e. This parameter has limited meaning considering that diffusion is only effective at high temperatures.

TABLE S1. Timescales and relevant variables of the dynamic modelling best-fitting curves based on linear and exponential cooling models.

Part 2: Relevant parameters and detailed calculations of minimum magma supply rate (Qc)

The minimal magma supply rate (Q_c) was calculated using Equation 4 of Morgado et al. (2017), which was modified based on the model (Eq. 1) of Menand et al. (2015).

$$Q_c = \frac{8}{9}\left(\frac{C_p(T_f - T_{inf})}{L(T_0 - T_f)}\right)^{\frac{9}{4}}\left(\frac{\Delta\rho g k^3 H^3}{\mu}\right)^{\frac{1}{4}}\left(\frac{K_c}{\Delta\rho g}\right)^{\frac{2}{3}}$$

Thermal analysis of magma transport particularly considers physical and thermal properties of the ascending magma (e.g., ascent height, initial and freezing temperature, latent heat) and country rock conditions (e.g., fracture toughness, thermal diffusivity, etc.). Where H is the depth from which magma can ascend to the surface without completely solidifying. In this case, we chose 20 km (maximum crystallization depth of the primitive olivine modelled by rhyolite-MELTS) which represents the maximum vertical distance that an ascending magma needs to travel before eruption for the Tianchi magmatic system. T_0 and T_f are the initial and freezing temperatures of the ascending magma, respectively. Crystallization temperatures of olivine cores (1138–1227 °C) calculated by Al-in-olivine thermometry (Coogan et al. 2014) were used to represent initial magma temperatures. We used rhyolite-MELTS to model a series of isobaric cooling models and evaluated the evolution of crystallinity with cooling temperature. The freezing temperature is defined as the temperature corresponding to the melt volume fraction of 0.6–0.7, representing the maximum particle packing fraction for magmas to retain the rheological properties of a melt (Cashman et al. 2017). The freezing temperatures range from 998 °C to 1121 °C for the considered pressure range resulting in temperature differences of 17 °C to 229 °C between the initial and freezing temperatures. $\Delta\rho$ is the density difference between the magma and the country rocks. We used the Tianchi average upper crust density of 2.65 g/cm^3 to represent the average density of country rocks (Guan et al. 2020). The density range of the ascending magma (2.39–2.65 g/cm^3) was assumed to correspond to the temperature evolution between initial and freezing magma temperature using rhyolite-MELTS.

DOI: https://doi.org/10.2138/am-2023-9296. http://www.minsocam.org/

μ is the dynamic viscosity of the ascending magma. To calculate μ, we first selected the corrected bulk-rock composition of TD-2 equilibrated with the Fo_{82} olivine (Part 5 of Appendix[1]) and the bulk-rock composition of LFZ-4 (Part 1 of Appendix[1]) representing the most primitive magma composition and the most evolved composition, respectively. Such compositions are employed in the equation of Giordano et al. (2008) to calculate the melt viscosity with no crystals. We calculate the melt viscosity as about 10 Pa•s based on a temperature of 1201 ℃ (olivine core average temperature of the TD unit) for the most primitive melt under the water content of 1 wt%, and about 114 Pa·s using a temperature of 1059 ℃ (clinopyroxene microlite average temperature of the LFZ unit) for the most evolved melt under the water content of 2.5 wt% (We assumed the water is perfectly incompatible, the initial water content is 1 wt% and the minimum melt fraction is 0.4). The dynamic viscosity of magma can be defined as the product of the melt viscosity combined with the effect of suspended crystals and vesicles (e.g., Harris et al. 2008):

$$\mu_{(magma)} = \mu_{(melt)} \times \mu_{(crystal)} \times \mu_{(vesicle)}$$

Here, we only consider the effect of suspended crystals, because vesicles are only present sparsely in our samples, and vesicles most probably formed after the eruption. The dynamic viscosity of the crystal-bearing magma was obtained using the equation of Krieger and Dougherty (1959) which considers the amounts of suspended crystals as well as crystal shapes. The crystal volume fraction was set to 5% of olivine and 10% of plagioclase. The olivine and plagioclase were assumed as spherical and prolate shapes respectively. Geometries of all crystals give the same magnitude of relative viscosity for a given crystal volume fraction ≤ 0.25 (Mueller et al. 2010). The maximum particle packing fraction is set as a melt volume fraction of 0.6-0.7 (Cashman et al. 2017). Therefore, the maximum magma dynamic viscosity is about 18.3–20.5 Pa·s for the most primitive melt and 182.7–205.3 Pa·s for the most evolved melt.

C_p is the specific isobaric heat capacity which ranges from 1300 J/kg K to 1700 J/kg K for natural silicate melts as suggested by Lesher and Spera (2015). L is the magma latent heat (2.5×10^5-5.5×10^5 J/kg), K_c is the fracture toughness of the country-rock ($10^6\times10^9$ Pa m$^{1/2}$), κ is the country-rock thermal diffusivity (0.3×10^{-6}-2×10^{-6} m^2/s) and T_{inf} is the crustal far-field temperature (50-600 °C) that represent the crustal temperature horizontally distal from the heat source. These values were taken from Menand et al. (2015) and references therein. g is the gravitational acceleration (9.8 m^2/s). Detailed ranges of all parameters are compiled in Table S2. We adopted the Monte Carlo simulation method to obtain the probability distribution of Q_c and the sampling number is 50,000 to ensure the reliability of the model results. Detailed modelled results of the expected range of critical supply rates for basaltic magmas are shown in Fig. S10. The Q_c presented in the main text define as the minimum boundary values of the complete range, i.e., the minimum magma supply rate for avoiding freezing of ascended magma in a ~20 km long dyke.

TABLE S2. Ranges of all parameters used in Monte Carlo simulations.

REFERENCES CITED

Ariskin, A.A., Barmina, G.S., and Frenkel, M.Y. (1986) Simulating low-pressure tholeiite-magma crystallization at a fixed oxygen fugacity, Geochemistry International, 24(5), 92–100.

Ariskin, A.A., Barmina, G.S., Frenkel, M.Y., and Nielsen, R.L. (1993) COMAGMAT: a Fortran program to model magma differentiation processes. Computers and Geosciences, 19, 1155–1170.

Beattie, P. (1993) Olivine-melt and orthopyroxene-melt equilibria. Contribution to Mineralogy and Petrology, 115, 103–111.

Giordano, D., Russell, J.K., and Dingwell, D.B. (2008) Viscosity of magmatic liquids: A model. Earth and Planetary Science Letters, 271, 123–134.

Guan, Y.W., Choi, S.C., Yang, G.D., Liu, J.Q., Lee, Y.S., Oh, C.W., Jin, X., and Wu, Y.G. (2020) Changbaishan Tianchi volcano crustal magma chambers modelling with gravity profile. Acta Petrologica Sinica (English Edition), 36, 3840–3852.

Harris, A.J.L., and Allen, J.S. (2008) One-, two- and three-phase viscosity treatments for basaltic lava flows. Journal of Geophysical Research: Solid Earth, 113, 1–15.

Klein, E.M. (2003) Geochemistry of the Igneous Oceanic Crust. In H.D Holland and K.K Turekian, Eds., Treatise on Geochemistry, p. 433-463. Pergamon Oxford.

Krieger, I.M., and Dougherty, T.J. (1959) A Mechanism for Non-Newtonian Flow in Suspensions of Rigid Spheres. Transaction of the Society of Rheology, 3, 137–152.

Lesher, C.E., and Spera, F.J. (2015) Thermodynamic and Transport Properties of Silicate Melts and Magma. In The Encyclopedia of Volcanoes (Second Edition), p. 113–141.

Mueller, S., Llewellin, E.W., and Mader, H.M. (2010) The rheology of suspensions of solid particles. Proceedings of the Royal Society A Mathematical Physical and Engineering Sciences, 466, 1201–1228.

Saunders, A.D., and Tarney, J. (1984) Geochemical characteristics of basaltic volcanism within back-arc basins. Geological Society, London, Special Publications, 16, 59-76.

Sun, S.S. (1980) Lead isotopic study of young volcanic rocks from mid-ocean ridges, ocean islands and island arcs. Philosophical Transactions of the Royal Society of London. Series A, Mathematical and Physical Sciences, 297, 409-445.

Sun, S.S., and McDonough, W.F. (1989) Chemical and isotopic systematics of oceanic basalts: implications for mantle composition and processes. Geological Society, London, Special Publications, 42, 313-345.

TABLES

TABLE 1.

unit	vesicular	mineral		size in diameter	volume percentage	morphology
TD	~5 vol.% in average	macrocryst	Ol	0.3-0.9 mm	~10-15 vol% in total, including dominant plagioclases followed by olivines	macrocrysts are euhedral to rounded, and skeletal microlites (100–200 µm) are also found
			Pl	0.2-2.7 mm		tabular
			Opx		never exist as a single macrocryst	
		glomerocryst	Opx + Pl	1.7-3.5 mm	rare, only three have been found in all TD samples	Pl and Opx are both euhedral
			Ol + Pl	0.7-1.9 mm	~1-5 vol% in total	Pl and Ol are both euhedral
BS	~5 vol.% in average	macrocryst	Ol	0.4-1.6 mm	~8-13 vol% in total, including dominant plagioclases followed by olivines	macrocrysts are euhedral to rounded, and skeletal microlites (100–200 µm) are also found
			Pl	0.2-3 mm		tabular
		glomerocryst	Ol + Pl	0.7-1.7 mm	~3-6 vol% in total	Pl and Ol are both euhedral
			Ol monomineralic cluster	0.8-1.3 mm	rare, only two have been found in all BS samples	euhedral to rounded

LFZ	~10-45 vol.% in average	macrocryst	Ol	0.2–0.7 mm	~3-25 vol% in total, vary largely among the thin sections	macrocrysts are euhedral to rounded, and skeletal microlites (100–200 μm) are also found
			Pl	0.2–3.3 mm		tabular
		glomerocryst	Ol + Pl	0.6-1.5 mm	~0-15 vol% in total, vary largely among the thin sections	Pl are tabular, Ol are euhedral to subhedral

1312 **TABLE 2.**

Equation		Relevant variable	Unit
(1) Diffusion accompanied by crystal growth and melt evolutionary —the moving and changing boundary	$\frac{\partial X_{Fo}}{\partial t}=\frac{\partial X_{Fo}}{\partial x}\left(D\frac{\partial X_{Fo}}{\partial x}\right)+G\frac{\partial X_{Fo}}{\partial x}$	(X_{Fo}) molar faction of the forsterite component→(2)	
		(G) growth rate→(4)	m/s
		(D) diffusion coefficient along profile→(5)	m^2/s
		(x) distance	m
		(t) time	s
(2) molar faction of the forsterite component	$X_{Fo}=Fo/100$	(Fo) forsterite content→ (3)	mol %
(3) Liquid line of descent	$Fo=f(T)$	[(f(T)] LLD function	mol %
		(T) temperature→(6)	K
(4) Gradually increasing growth rate	$G=2G_0\left(\frac{T_0-T}{T_0-T_{min}}\right)$	(T_0) diffusion initial temperature	K
		(T_{min}) diffusion finial temperature	K
		(G_0) half-growth rate at Gmin	m/s
(5) diffusion coefficient along profile	$D=D_{[001]}cos^2\alpha+D_{[010]}cos^2\beta+D_{[001]}cos^2\gamma$	($D_{[001]}$) Fe–Mg interdiffusion coefficient in olivine along [001] axis→(7)	m^2/s
		($D_{[010]}$) Fe–Mg interdiffusion coefficient in olivine along [010] axis→(8)	m^2/s
		($D_{[100]}$) Fe–Mg interdiffusion coefficient in olivine along [100] axis→(8)	m^2/s

This is the peer-reviewed, final accepted version for American Mineralogist, published by the Mineralogical Society of America.
The published version is subject to change. Cite as Authors (Year) Title. American Mineralogist, in press.
DOI: https://doi.org/10.2138/am-2023-9296. http://www.minsocam.org/

		(α, β, and γ) The angles between the profile direction and the principal axes	
(6) Constant cooling rate	$T = T_0 - qt$	(q) constant cooling rate	K/s
(7) Fe–Mg interdiffusion in olivine	$D_{[001]} = 10^{-9.21} * (\frac{fO_2}{10^{-7}})^{\frac{1}{6}} * 10^{3(0.9-X_{Fo})} * exp(-\frac{E_{Fo} + 7 * 10^{-6} * (P - 10^5)}{RT})$	(fO_2) oxygen fugacity→(9) (P) pressure (R) Universal gas constant (E_{Fo}) the Fo activation energy at 10^5 Pa	Pa Pa J/(mol·K) J/mol
(8) The relationship between $D_{[001]}$, $D_{[010]}$, and $D_{[100]}$	$D_{[001]} = 6D_{[010]} = 6D_{[001]}$		
(9) Ni-NiO oxygen fugacity buffer	$log(fO_2) = \frac{12.78 - 25073/T - 1.1logT + 4.5 * 10^8P/T + 25000P}{10^5}$		

TABLE S1

Unit	Sample name	Line	Cooling model	T_0 (K)	T_{min} (K)	Cooling rate (m/s)	τ (days)	(G_0)	r^2	time (days)
TD	TD-2A-Ol1	2	Linear cooling	1432	1377	1.6223E-06		5.474E-13	0.997	403.7
			Exponential cooling	1433	1369		9803.0	5.739E-13	0.995	433.0
	TD-3A-Ol1	1	Linear cooling	1457	1374	1.71003E-06		9.139E-13	0.999	560.2
			Exponential cooling	1453	1373		10028.5	8.375E-13	0.999	584.0
	TD-3B-Ol2	1	Linear cooling	1443	1380	5.17354E-06		3.807E-13	0.998	421.3
			Exponential cooling	1430	1380		9961.8	1.349E-13	0.948	365.0
	TD-4A-Ol1	1	Linear cooling	1435	1363	1.25055E-06		4.266E-13	0.999	674.3
			Exponential cooling	1443	1364		11631.2	4.73E-13	0.998	672.0
	TD-4B-Ol2	1	Linear cooling	1415	1371	1.10515E-06		4.693E-13	0.999	471.8
			Exponential cooling	1429	1374		10665.8	6.212E-13	0.999	428.0
	TD-4C-Ol2	1	Linear cooling	1429	1369	1.24936E-06		1.362E-13	0.999	562.5
			Exponential cooling	1439	1369		11579.4	1.671E-13	0.999	593.0
BS	BS-2A-Ol1	1	Linear cooling	1460	1372	2.22727E-06		6.985E-14	0.998	469.3
			Exponential cooling	1465	1371		6472.8	9.076E-14	0.999	442.0
	BS-5A-Ol1	1	Linear cooling	1441	1371	1.7787E-06		4.266E-13	0.998	466.6
			Exponential cooling	1441	1371		11375.7	2.57E-13	0.997	543.0
	BS-5B-Ol1	1	Linear cooling	1457	1360	2.48352E-06		5.502E-13	0.998	465.9
			Exponential cooling	1442	3819		8432.5	3.111E-13	0.999	504.0
	BS-7A-Ol3	1	Linear cooling	1409	1352	9.55156E-07	`	5.562E-13	0.995	572.8
			Exponential cooling	1424	1352		10510.1	8.405E-13	0.999	561.0
	BS-7B-Ol5	1	Linear cooling	1463	1366	1.76166E-06		7.761E-14	0.998	645.9
			Exponential cooling	1462	1365		9193.5	8.664E-14	0.999	595.0

TABLE S2

Parameter		Range	Unit
H	height	20000	m
T_0	initial magma temperature	1138-1227	℃
T_f	freezing magma temperature	998-1121	℃
$\Delta\rho$	density contrast	1-260	kg/m^3
μ	magma dynamic viscosity	18.3-205.3	Pa·s
C_p	isobaric heat capacity	1300-1700	J/kg K
L	magma latent heat	2.5×10^5-5.5×10^5	J/Kg
K_c	fracture toughness	10^6-10^9	Pa $m^{1/2}$
κ	thermal diffusivity	0.3×10^{-6}-2×10^{-6}	m^2/s
T_{inf}	crustal far-field temperature	50-600	℃
g	gravitational acceleration	9.8	m^2/s

DOI: https://doi.org/10.2138/am-2023-9296. http://www.minsocam.org/

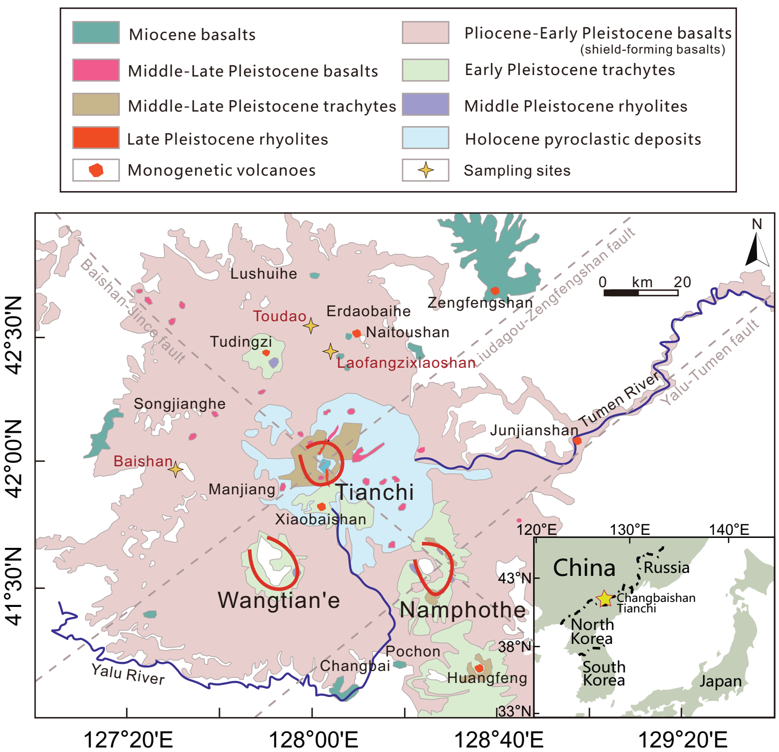

Fig 1

DOI: https://doi.org/10.2138/am-2023-9296. http://www.minsocam.org/

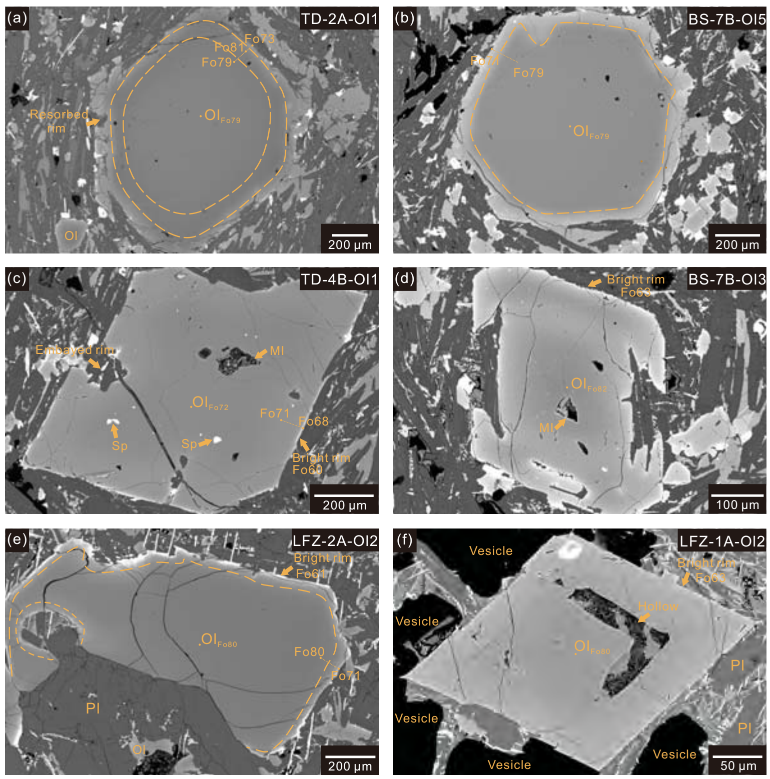

Fig. 2

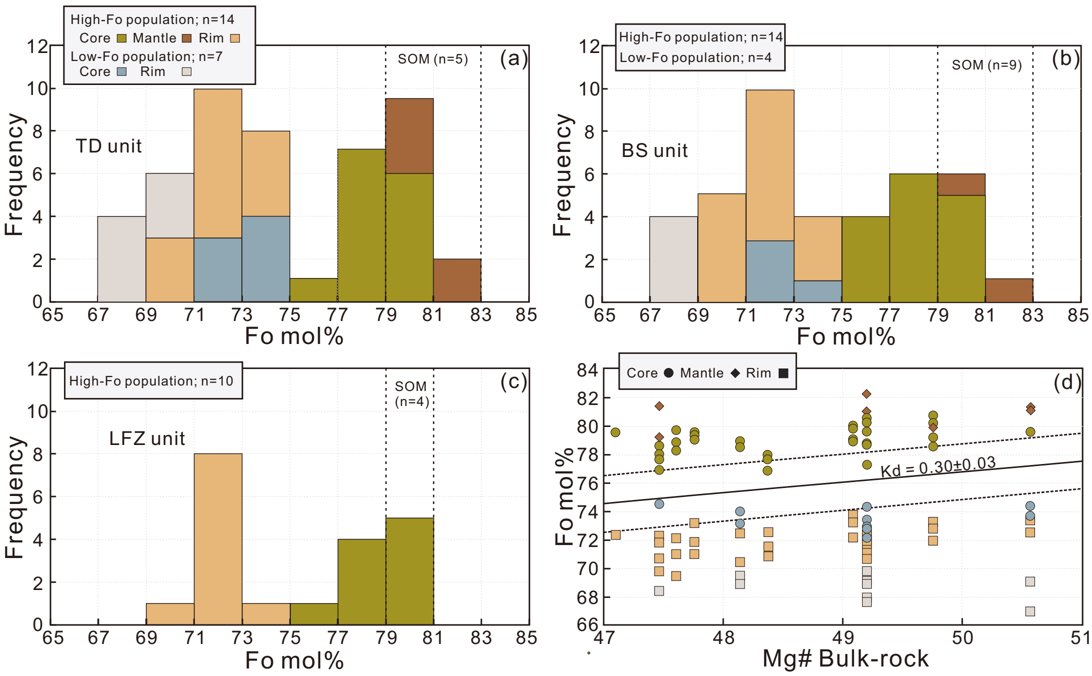
High-Fo population; n=14
Core Mantle Rim
Low-Fo population; n=7
Core Rim
SOM (n=5)
(a)
TD unit
Frequency
Fo mol%
High-Fo population; n=14
Low-Fo population; n=4
SOM (n=9)
(b)
BS unit
High-Fo population; n=10
SOM (n=4)
(c)
LFZ unit
Core Mantle Rim
(d)
Kd = 0.30±0.03
Fo mol%
Mg# Bulk-rock

Fig 3

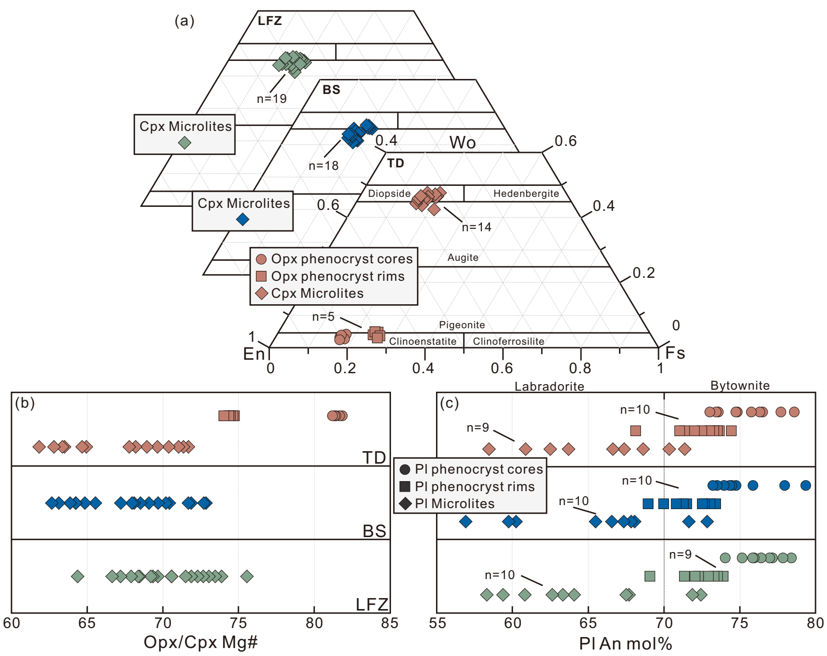
(a)
LFZ
BS
TD
Cpx Microlites
Wo
En
Fs
Diopside
Hedenbergite
Augite
Pigeonite
Clinoenstatite
Clinoferrosilite
n=19
n=18
n=14
n=5
Opx phenocryst cores
Opx phenocryst rims
Cpx Microlites
(b)
Opx/Cpx Mg#
(c)
Labradorite
Bytownite
Pl phenocryst cores
Pl phenocryst rims
Pl Microlites
n=10
n=9
Pl An mol%

Fig 4

DOI: https://doi.org/10.2138/am-2023-9296. http://www.minsocam.org/

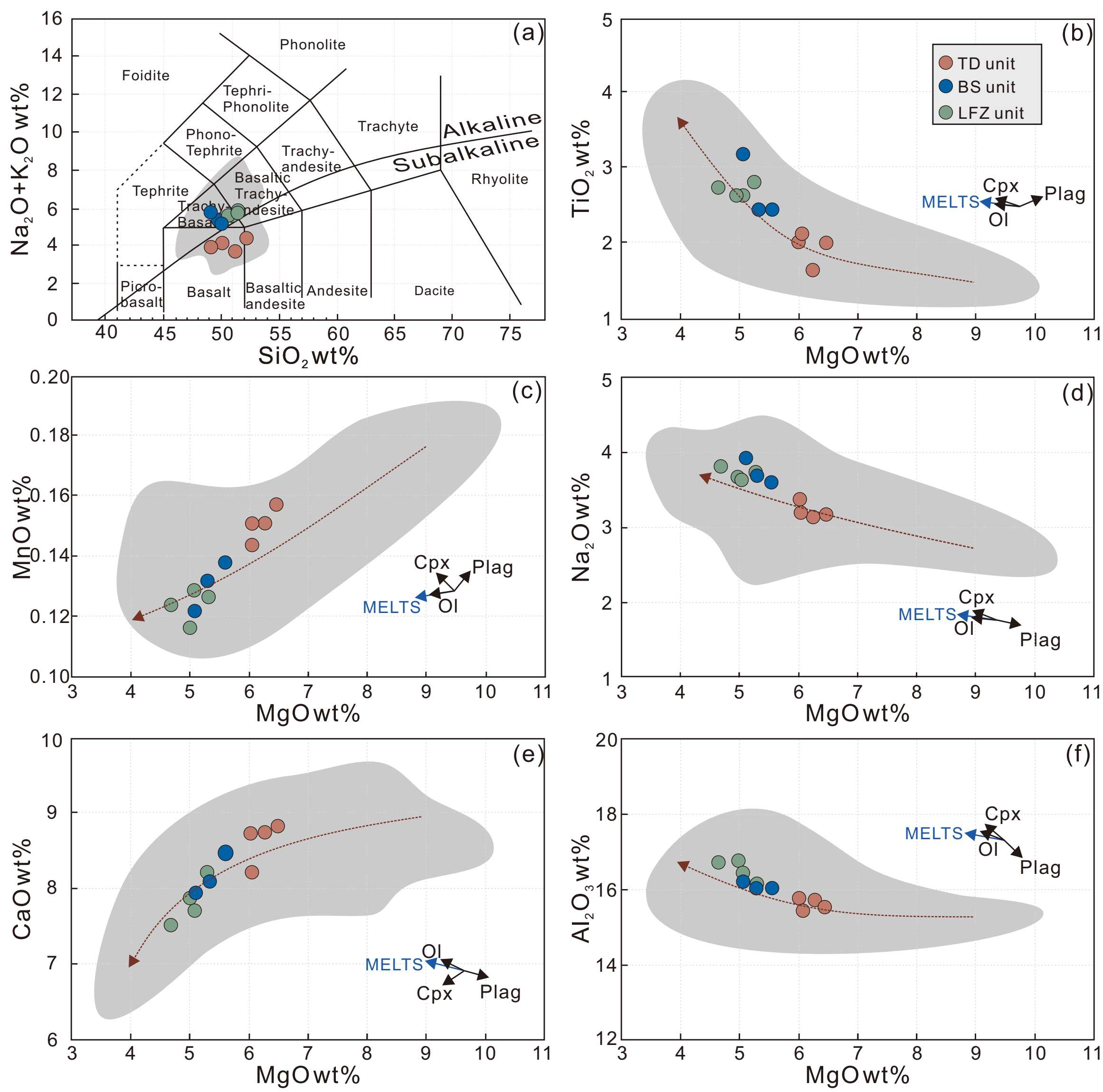

Fig 5

DOI: https://doi.org/10.2138/am-2023-9296. http://www.minsocam.org/

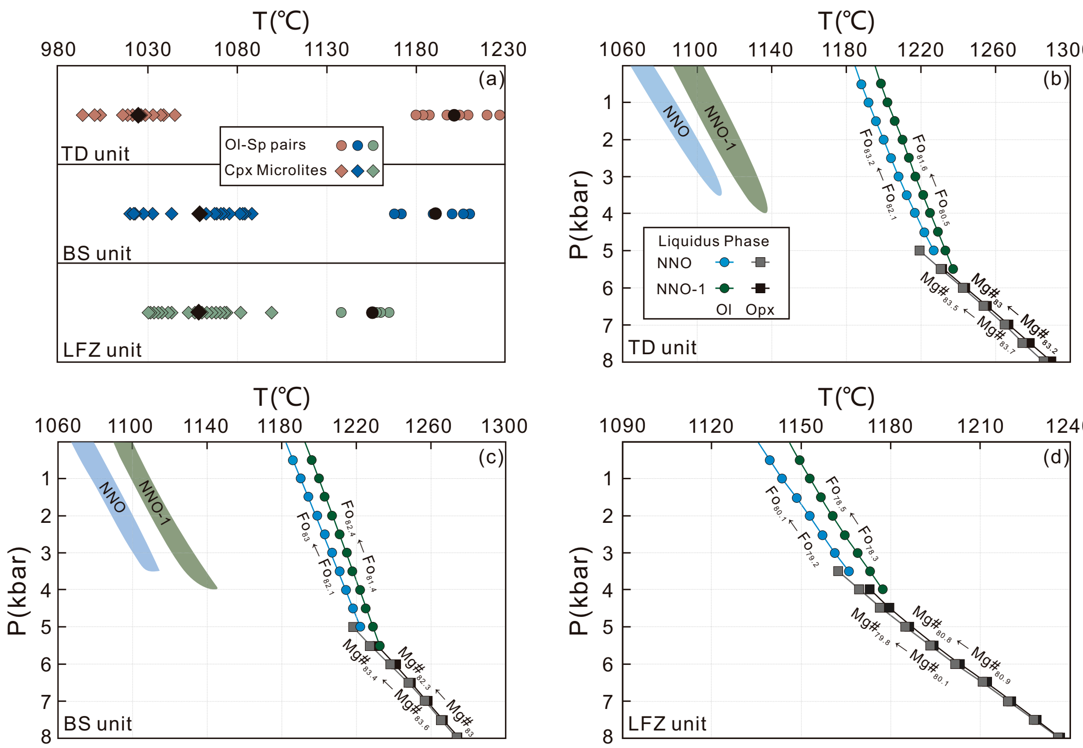

Fig 6

DOI: https://doi.org/10.2138/am-2023-9296. http://www.minsocam.org/

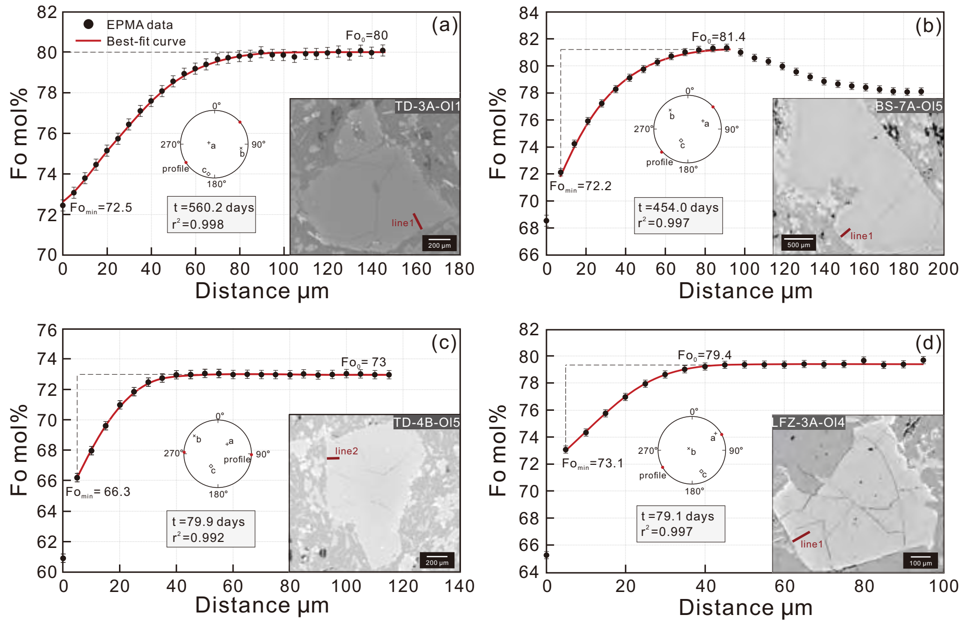

Fig 7

DOI: https://doi.org/10.2138/am-2023-9296. http://www.minsocam.org/

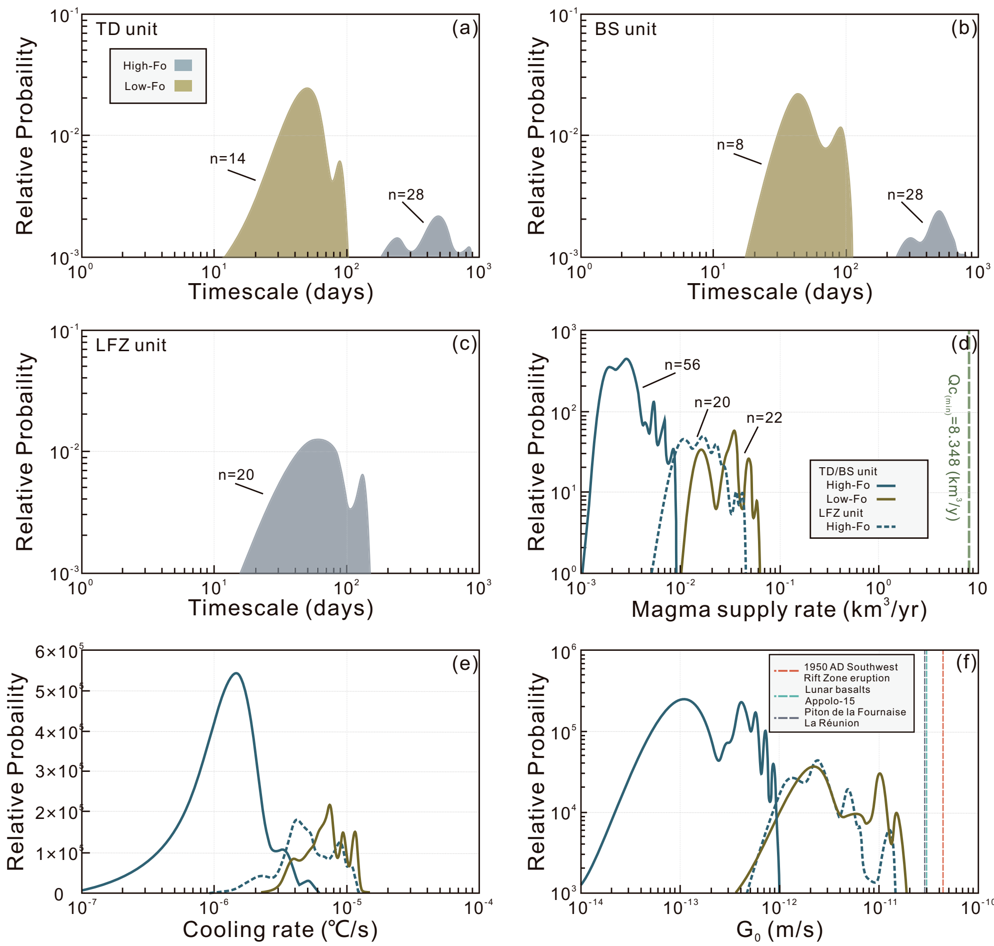

Fig 8

DOI: https://doi.org/10.2138/am-2023-9296. http://www.minsocam.org/

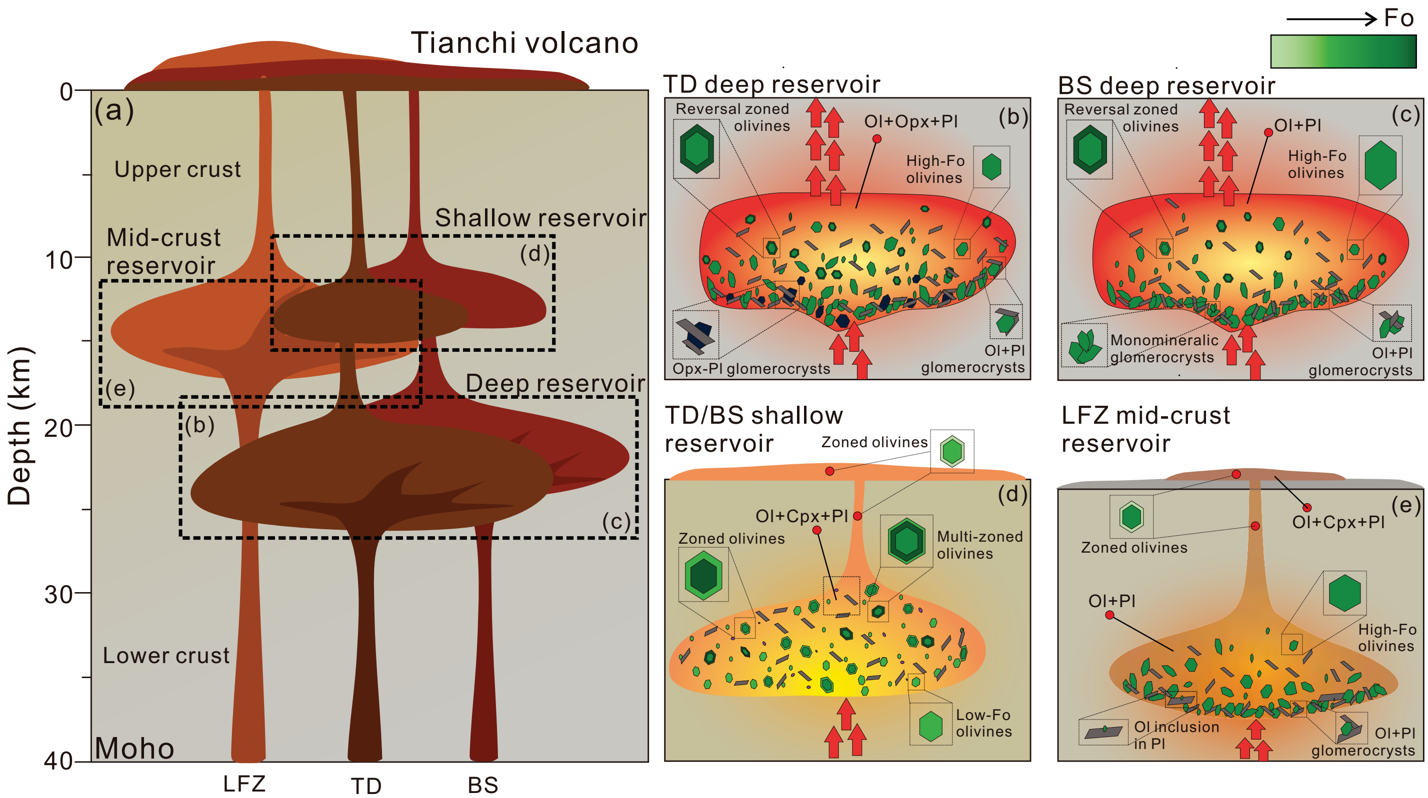

Fig 9